12-2019

Quantitative Study of the Antimicrobial Effects of Silver on the Motility of Escherichia coli

Benjamin Russell
University of Arkansas, Fayetteville

Quantitative Study of the Antimicrobial Effects of Silver on the Motility of *Escherichia coli*

A thesis submitted in partial fulfillment
of the requirements for the degree of
Master of Science in Physics

by

Benjamin Russell
California Lutheran University
Bachelor of Science in Physics, and Mathematics, 2017

December 2019
University of Arkansas

Yong Wang, Ph.D.
Thesis Chair

Pradeep Kumar, Ph.D.
Committee Member

William Lin Oliver, Ph.D.
Committee Member

Woodrow Shew, Ph.D.
Committee Member

Abstract

In recent decades, the number of antibiotic-resistant bacterial infections has grown to become a serious global threat. This rise can be attributed to the widespread misuse of antibiotics and the lack of newly developed drugs to fight resistant organisms. Novel bactericidal substances have, therefore, garnered significant research interest. Silver, due to its powerful antimicrobial effects, is one such substance. Silver is typically most effective in cationic form; however, advancements in nanotechnology have paved the way for the controlled fabrication of nano-silver. Silver nanoparticles have been shown to have increased antibacterial potency for a variety of reasons, including the release of silver ions into aqueous media. Nonetheless, the entire antimicrobial mechanism of silver nanoparticles has not been completely elucidated. One such unexplored interaction is with bacterial motility. Motility allows bacterial cells to navigate their environment and steer themselves in favorable directions. Furthermore, motility has been shown to play an important role in virulence and biofilm-formation.

In this research, I investigated the interactions between silver ions and motility of *Escherichia coli*. By performing and collecting data from a series of phase-contrast microscopy experiments, I was able to show, through quantitative modeling and results, that silver ions cause a decrease in swimming velocity, an increase in tumbling frequency, and an increase in tumbling dwell time, all while not killing the cell. The experiments I performed included free-swimming experiments, in which bacteria swam in the 2-D focal plane, and tethering assay experiments, where a cell was trapped to a glass coverslip by a single flagellum. By modeling the rotational velocity of the tethered cells using hidden Markov models, I was able to show that silver ions cause a significant change to the tumble-to-run probabilities of treated cells. These results are of great importance for furthering the understanding of silver as a bactericide.

Acknowledgments

Thank you to Dr. Wang for giving me the opportunity and constant support to pursue this research. Thank you to my lab mates and friends for making the past two years such a fun and enriching experience. Thank you to my wife and best friend, Alyssa, for pushing me to be a better person and making everyday just a little better. Thank you to Mom, Dad, Cam, Maddie, Sheila, Dan, and Kristen for all loving me so much and helping me to get to this point. (Thank you to Bootsy boy, too.)

Contents

1 Introduction

1.1 The Antibiotic Resistance Crisis

Since the discovery of penicillin, antibiotics have saved countless lives from infectious diseases [1–3]. With their introduction into medicine, antibiotics have helped to reduce childhood mortality, increase life expectancy, and improve the outcomes of clinical surgery [1–3]. However, the universal efficacy of these "miracle-drugs" has dwindled in recent decades as increasing numbers of infectious species have developed resistance to one or more antibiotics to which they were previously susceptible [1,2]. Emerging antibiotic-resistance is due largely to overuse and misuse in the clinical and agricultural settings [2,3]. As a result, the number of infections in the United States due to antibiotic-resistant pathogens is around two million per year and increasing [1,2]. Despite this, the number of new antibiotics introduced and in development has decreased over the past few decades [1–3]. Most pharmaceutical companies do not invest resources in antibiotic research due to the drugs' low costs, opaque regulatory barriers, and the short treatment duration [3]. Furthermore, any newly developed drugs are used as a last resort for fear of increasing the likelihood of resistance [3]. The resulting lack of investment has been met with an estimated $20 billion cost on the American health care system and an estimated $35 billion in lost productivity and wages annually [3]. In combatting this global threat, renewed research efforts into new antibiotic agents and their mechanisms, along with implementation of best-practices, are of dire importance [2–4].

1.1.1 History

In 1928, Alexander Fleming found that penicillin, a substance produced by a fungus from the Penicillium genus, possessed strong bactericidal and inhibitory properties against staphylococcus bacteria [1,5]. His discovery, and the later production of penicillin for clinical use in the 1940s, ushered in a new era of medicine in which antibiotic substances produced by organisms could be used to fight infectious diseases in humans [1]. The following decades

saw the introduction of a swath of natural antibiotics such as streptomycin, tetracycline, and vancomycin as well as classes of synthetic drugs like the sulfonamides [1]. The mortality rate due to pneumonia, influenza, and tuberculosis fell abruptly between the 1940s and 50s thanks in part to effective antibiotics [6]. Penicillin, in particular, proved to be instrumental in curing life-threatening diseases during World War 2 [1].

However, only a few years after their introduction into medicine in the 1930s, sulfonamides began losing efficacy due to resistance [4]. For penicillin, enzymes enabling resistance were found in bacteria before the drug was introduced as a therapeutic [4,7]. Even more alarming was the discovery of resistance-genes in 30,000-year-old bacterial DNA [8]. These genes could code for resistance to a diverse set of antibiotics including β-lactams, tetracyclines, and glycopeptides like vancomycin, a drug previously thought to be too difficult to attain resistance to in a clinical setting due to its multi-faceted antibacterial mechanism [3, 8]. These discoveries demonstrate that antibiotic-resistance is an ancient enemy that, through the overuse and misuse of antibiotics, has been given new life.

1.1.2 Killing-Mechanisms of Antibiotics

Antibiotics of different classes can affect susceptible organisms in a variety of ways. Aminoglycosides, tetracyclines, macrolides, and phenicols inhibit translation in some bacteria [4]. Streptomycin, a member of the aminoglycosides, binds to the 30S ribosomal subunit and disrupts protein synthesis [9]. Other classes, such as the β-lactams and glycopeptides, target peptidoglycan biosynthesis by binding with enzymes in the cytoplasmic membrane known as penicillin-binding proteins (PBPs) [10]. This mechanism inhibits cell division and growth eventually leading to cell death [10]. Still others like ciprofloxacin, a fluoroquinolone, target replication via inhibiting bacterial DNA from unwinding and duplicating [11].

1.1.3 Mechanisms of Resistance

The killing-mechanisms of a particular antibiotic will not necessarily be effective against all bacteria. Vancomycin, for instance, cannot cross the outer membrane of Gram-negative bacteria [2]. Gram-negative bacteria, therefore, possess intrinsic resistance to vancomycin. There are some cases in which intrinsic resistance can be overcome. For example, multiple antibiotics can be used in concert; one antibacterial agent can inhibit an intrinsic resistance mechanism while another enacts its default mechanism against its target [2]. Acquired or developed resistance, on the other hand, refers to a mechanism or set of mechanisms of an organism that deactivate an antibiotic to which the organism is not intrinsically resistant. Some of these mechanisms include modifying the antibiotic target causing decreased affinity, reducing the intracellular concentration of the antibiotic via efflux or resisting penetration, or employing enzymes to hydrolyze or otherwise modify the antibiotics [2].

β-lactamases, the enzymes responsible for conferring resistance to penicillin and other β-lactams, are widespread on a global scale [4]. Organisms producing these enzymes can be found in human and animal intestinal tracts, in clinical settings, and in the environment [12]. The genes that code for these enzymes are ancient and quickly mutate, thus creating a diverse set of resistance pathways [4]. The macrolide antibiotics, introduced to fight multi-drug resistant *Staphylococcus aureus* (MRSA), disrupt translation by binding to sites in the peptide exit tunnel of the 50S ribosome subunit [4]. Resistance, then, has been seen to be manifested by a change to the RNA or protein components of this tunnel, decreasing binding affinity [4]. Fluoroquinolones, effective against various Gram-negative bacteria, can be rendered useless by mutations in the targeted gyrase gene accompanied with increased efflux of the drug [4]. In addition to intrinsic resistance as a result of morphology, intrinsic resistance can refer to the existence of genes that could result in a resistant phenotype. Over-expression of these otherwise silent genes can lead to resistance, as is the case for sulfonamides and trimethoprim [4].

Antibiotic-producing bacteria and fungi can be sources of resistance genes (r genes) for

pathogens [4]. These genes can be mobilized on plasmids and exchanged among peers via horizontal gene transfer (HGT) or passed from parent to offspring via vertical gene transfer. HGT can be enacted via conjugation in which plasmids are transferred between cells across connecting pili. This has been found to occur frequently in human and animal guts, leading to the prevalence of diverse r genes therein [4]. Transformation refers to the process by which cells release DNA in the form of plasmids to be up-taken later by competent cells. Once captured, these plasmids can exist separate from or integrated into the genome of the host. *Acinetobacter* spp. are naturally competent and thus HGT in this way is common [4].

1.1.4 Efforts to Overcome Antibiotic Resistance

The selection pressure of modern antibiotics is much greater than at any time during the pre-antibiotic era [4]. Human production of antibiotics is the largest source of antibiotics in the environment [4] and the prevalence of these drugs has had dire consequences. Antibiotics see extensive use across disparate fields like agriculture as growth promoters and for pest control, or therapeutically in humans, or in research and industry [4]. Pollution from manufacturing, wastewater, and runoff from animal husbandry sites have not only lead to alterations of the gut microbiome of local animals and humans, but have also created breeding pools for r genes and resistant organisms [4, 13].

To curb this crisis, many countries have enacted preventative policies. In the 1990s, to address rising rates of infection in patients, Iceland, Finland, France, Greece, and the United States each enacted restrictive policies that limited the use of antibiotics against resistant organisms [14]. Each time, rates of infections, mortality, and lengths of stay were seen to decline as the selection pressure for those resistant organisms decreased. More recently, government bodies have placed policies into effect that limit the use of antibiotics in the agricultural industry. In 2012, the FDA outlined policies concerning the judicious use of antibiotics in livestock production. Among these provisions was a call to eliminate the inclusion of sub-therapeutic concentrations of antibiotics in feed and water, and, as of 2014,

all producing companies have heeded the FDA's guidelines [15]. In the 1970s, after the findings that antibiotic resistance among humans was related to antibiotic use in livestock from the Swann Report, penicillin and tetracycline were banned as growth promoters in the United Kingdom [15]. In the 1980s and 1990s, other European nations began banning individual antibiotics as growth promoters if not banning all antibiotics for non-therapeutic use altogether. In 2006, an EU-wide ban was placed on all antibiotics as growth promoters [15]. The use of antibiotics for curative purposes, however, persists albeit with greater regulation [15]. Despite the implementation of best-practices and governmental oversight, the problem of antibiotic-resistant infections continues to grow.

The past twenty years have been hallmarked by failures of modern techniques to produce any new classes of antibiotics [16]. Modern antibiotic discovery is focused on targeting essential genes that are not protected by known resistance mechanisms [16]. These methods have, however, been impeded by their inability to produce broad-spectrum agents or agents active against Gram-negative bacteria, due to their thicker peptidoglycan layer [16]. Furthermore, single-target approaches can be more susceptible to emergent resistance [16].

Another roadblock in fighting antibiotic-resistance is the steady decline of industry involvement in the research and development of new antibiotic substances [3, 17]. In order to spark initiative and innovation within this field, the Infectious Disease Society of America (IDSA) proposed a multi-faceted plan that included refactored regulations and bolstered economic incentives [17]. Fortunately, as of 2018 there now over 58 distinct initiatives on national, global, and EU levels whose goal is to promote antibiotic drug development [18]. These movements include The Joint Programming Initiative on Antimicrobial Resistance (JPIAMR), the Combating Antibiotic Resistant Bacteria Biopharmaceutical Accelerator (CARB-X), the Global Antibiotic Research and Development Partnership (GARDP), the Global Antimicrobial Resistance Innovation Fund (GAMRIF), the EU's Innovative Medicines Initiative and its subsidiary New Drugs for Bad Bugs (ND4BB) Program, and the US's Biomedical Advanced Research and Development Authority (BARDA) [18].

1.2 Silver as an Antibacterial Substance

As the demand for a solution to antibiotic-resistant pathogens has grown, so too has the interest in metal nanoparticles as antibacterial agents. Silver nanoparticles, in particular, have attracted a large amount of research resources due to their reproducible and versatile production methods, high specific surface area, and their intrinsic antimicrobial effect stemming from the release of silver ions into aqueous solutions. Although research interest in silver is only recently growing, silver has been known to possess bactericidal properties for millennia [19–21]. Herodotus, an ancient Greek historian (c. 484 BCE), noted that the Persians stored water in silver containers to prevent contamination [19,21]. Now, with the capabilities of nanotechnology, silver nanoparticles can be fashioned into a variety of structures including nanocubes, nanowires, and nanospheres [21]. Furthermore, silver nanoparticles have shown efficacy against Gram-negative bacteria as they are able to bind and interfere with the cell wall [19, 21].

1.2.1 History

Empirically, silver has been known to possess antibacterial properties for over six thousand years [20]. Civilizations reaching back in time as far as the ancient Egyptians, and as recently as the North American pioneers have all used silver for water filtration [20, 21]. In times of plague, the use of silver cutlery was seen to be associated with lower rates of infection [20].

For medical use, silver nitrate ($AgNO_3$) has seen extensive application in preventing infection in wounds since the 16^{th} century [19]. While this practice still exists today, silver is often replaced by or used in conjunction with antibiotics [19, 20]. In the 1800s, it was discovered that silver's primary mode of action is the release of silver ions [19]. In 1881, Dr. Carl Siegmund Franz Credé introduced the use of a 1% silver nitrate solution against opthalmia neonatorium, an ocular disease in newborn infants [19–21]. His method was successful (reduced occurrence from 7.8% to 0.13% in 13 years) and became a globally accepted form of treatment. His son, B.C. Credé, demonstrated that colloidal silver could

be used to treat wound sepsis [19, 20]. Halsted, an early 20th century American surgeon, employed silver-containing sutures to prevent infections in surgical incisions [20].

However, after the introduction of penicillin into the clinical setting in the 1940s, use of silver for the treatment of bacterial infections decreased. Nonetheless, its use remained and, in 1965, Moyer introduced the use of 0.5% silver nitrate for the treatment of burn wounds [19]. Later, in 1968, silver sulfadazine cream was created by combining silver nitrate with sulfonamide antibiotics [19]. This cream serves as a broad-spectrum antimicrobial for the treatment of burns [19]. In addition to topical use, oral consumption of silver colloids was clinical practice in the early 1900s [21]. In low doses, silver is seen to be largely harmless. However, ingestion can cause argyria (harmless blue-gray discoloration of the skin) and other complications [19–21]. More recently, nano-silver has been used as a coating for medical devices such as catheters, needles, and bandages [21]. Beyond its use for medical applications, silver has seen an uptick of use in consumer products such as textiles, cosmetics, and home appliances [21, 22].

1.2.2 Silver Ions and Nanostructures

Alexander, in his extensive review of the medical history of the use of silver, claims that the discovery of the release of silver ions (Ag^+) as the primary antibacterial mode of action of silver was made by Vonnaegele in the 19th century [20]. Vonnaegele found that silver displayed antimicrobial effects against at least 650 different organisms [20]. Ag^+ can be obtained by dissolving $AgNO_3$ in aqueous solutions or by oxidation of metallic silver [21].

Silver nanoparticles (AgNPs) refer to clusters of silver atoms whose diameter in any dimension is between 1 and 100 nanometers. AgNPs can be synthesized by "bottom-up" methods which involve agents such as citrate, glucose, ethylene glycol, or sodium borohydride reducing Ag^+ to form AgNPs [21, 23]. Physical methods fall under the "top-down" classification of synthesis methods [23]. Here, bulk material is ground down and subsequently stabilized. Physical reduction methods include optical quantum reduction and microwave

reduction of $AgNO_3$ [22]. Chemical synthesis methods are typically high-yield but produce hazardous by-products [23]. Conversely, physical methods produce fewer harmful chemicals but also result in lower yields and consume high amounts of energy [23]. Biological synthesis, on the other hand, has been found to be a "green" alternative to chemical or physical reduction methods due to the mild nature of the involved substrates and reaction [22]. Synthesis in this way relies on microorganisms capable of reducing Ag^+ to AgNPs [22]. Biological synthesis is simple, rapid, and non-toxic all while being flexible enough to produce particles of a desired size and morphology in a high-yield fashion [22, 23].

1.2.3 Known Mechanisms

While the antimicrobial mechanism of silver has yet to be completely characterized, many interactions between silver substances and bacterial cells have been reported in the literature. Much of the antibacterial activity of cationic silver stems from its interactions with the negatively charged bacterial cell wall [24]. *E. coli* and *S. aureus* treated with $AgNO_3$ were seen to undergo morphological changes during which the cytoplasmic membrane detached from the cell wall [25, 26]. Additionally under these conditions, silver ions can be found to bind to the negatively charged nucleic acids of the cell [27]. In response, DNA molecules were found to condense in an effort to protect genetic information from damage [25, 26]. Silver ions were also found to bind with sulfhydryl groups causing deactivation of essential respiratory enzymes [25,28]. Other negatively charged functional groups such as phosphates, hydroxyls, imidazoles, and indoles were also targets [27]. Ultimately, these effects resulted in mutations to the cell wall and membrane leading to cell lysis and death [24, 27].

Silver nanoparticles exhibit similar interactions. However, due to their high surface area to volume ratio, AgNPs possess greater antibacterial efficiency [19, 25]. Against Gram-negative bacteria, AgNPs were seen to attach to and penetrate the cell membrane causing intracellular release of silver ions [29,30]. AgNPs with a positive zeta potential were seen to interact with the negatively charged bacterial exterior at a higher rate [27]. This, in addition

to the physical antimicrobial properties of silver nanoparticles, made them more effective than cationic silver or their neutral and negatively charged counterparts [27]. Although the literature contains mixed conclusions, it has also been shown that AgNPs may intercalate into DNA thus interfering with transcription and translation [27]. Additionally, AgNPs release reactive oxygen species (ROS) into the cell cytoplasm [27]. These form highly reactive free radicals with high bactericidal activity [27]. Ribosomal damage is another marker of AgNP interaction with bacteria [27].

The antibacterial properties of AgNPs are dependent on size, shape, and concentration [27]. This variability provides more options than were available with silver ions when designing nanoparticles for therapeutic purposes. Against *E. coli*, triangular AgNPs were efficient even at low concentrations. A typical concentration that was effective against a wide class of pathogens, including the most hardy species, was around 75 μg/mL [27]. When used along side antibiotics AgNPs showed great results. The minimum inhibitory concentration (MIC) of the antibiotics used was decreased and the AgNPs assisted in rendering the bacteria susceptible to antibiotic treatment [27]. When tested against vancomycin- and trimethoprim-resistant bacteria, the synergistic effects of AgNPs with antibiotics increased the susceptibility from 20 to 30% [27].

Biofilm-producing pathogens, of which *E. coli* is one, have been found to be one of the leading causes of chronic infectious diseases such as cystic fibrosis, endocarditis, and periodontal diseases [27]. Biofilms consist of a community of bacteria attached to a solid surface. This formation is housed within a polymeric solution of DNA, proteins, and polysaccharides excreted by the formerly planktonic cells. These commonly develop in aqueous environments such as on water pipes, teeth, and medical devices [27]. Biofilms offer the enclosed cells greater access to substances key for metabolism and survivability. Biofilms are more capable of evading host defenses, engaging in horizontal gene transfer, and proliferating via partial detachment of the biofilm. Antibiotics struggle to defend against biofilm formation because the extracellular matrix limits their diffusion. AgNPs, however, have been shown

to infiltrate this complex. Against *Pseudomonas aeruginosa*, AgNPs caused anywhere from a 65 to 88% reduction in biofilm formation over 48 hours when used at micromolar concentrations [27]. The use of AgNPs in prostheses such as dental implants and bone cement has been shown to cause a decrease in *S. mutans* biofilm formation.

1.2.4 Limitations

Developed resistance to silver is very rare owing to silver's multi-faceted antibacterial mechanism [27]. Additionally, its low cytotoxicity makes silver a strong candidate for therapeutic use either with or in place of traditional antibiotics. Although there has been some use of silver in medical and consumer products, its adoption has not been resounding. Governing bodies in the USA and Europe have expressed concerns over potential human risk factors associated with the presence of silver in commercial products [21]. The reasons for this alarm stem from unexplored cytotoxicity factors and potential adverse environmental effects [21]. Futhermore, it is crucial to understand how bacteria may develop resistance, if possible, before expanding the use of silver and silver nanoparticles.

Oral consumption or exposure to silver nanoparticles can lead to massive release of silver ions in the gastrointestinal tract [22]. This contact has been found to be associated with hepatotoxicity (liver damage), apoptosis, and inflammation [22]. Silver's main targets in the human body are the spleen, liver, and kidneys [22]. Silver miners exposed to low doses of silver dust or soluble silver at or below threshold limits were seen to be free from adverse health effects [22]. They are, however, more likely to develop argyria.

Silver-resistant bacteria have been found in silver mines [31]. These bacteria can accumulate up to 25% of their mass in the form of silver on their exterior [31]. In fact, these same bacteria can be used for the biosynthesis of silver nanoparticles [31]. It remains unclear, however, how the use of silver and silver nanoparticles in consumer products selects for resistance among pathogenic bacteria [21].

Despite these limitations, silver nanoparticles' broad-spectrum bactericidal properties

and cost-effective manufacturing [32] align well with the industry and governmental expectations for antibiotics.

1.3 *E. coli* as a Model Organism

Escherichia coli is a Gram-negative, rod-shaped bacterium commonly found in the lower intestinal tract of warm blooded animals such as humans and cattle [33]. As a commensal, *E. coli* can provide the host with a swath of benefits including the production of vitamin K_2 [34] and prevention of infection from foreign pathogens [35]. However, some *E. coli* strains are dreadful human pathogens that can lead to diseases resulting in severe inflammatory responses and even death [33]. It is estimated pathogenic *E. coli* infections are responsible for more than two million annual deaths worldwide [33]. This problem is only exacerbated by the growing occurrence of antibiotic-resistant strains.

In addition to its importance as a pathogen, *E. coli* is also one of the most well-studied bacterium with regards to motility [33]. Motility allows for the exploration of the cell's environment in order to acquire necessary substances and avoid deleterious ones. The chemotactic system that controls the motility of *E. coli* has been thoroughly investigated in both the molecular and cellular regimes [36]. Therefore, *E. coli* provides a well-studied model system in order to investigate the effects of silver on motility.

1.3.1 As an Infectious Agent

Pathogenic *E. coli* cause persistent diarrhea which remains one of the highest causes of death for children 5 years of age and younger [37]. Pathogenic strains can be subdivided into at least these six classes based on their means of infection and symptoms [33, 38]:

- Shiga toxin-producing *E. coli* (STEC): produce the Shiga toxin which causes severe gastrointestinal illness. The Shiga toxin causes diarrhea and hemolytic uremic sydrome, a life-threatening complication hallmarked by symptoms such as thrombocytopenia, hemolytic anemia, and kidney failure [37, 38].

- enteropathogenic *E. coli* (EPEC): major cause of diarrhea in infants in developing countries [37].
- enterotoxigenic *E. coli* (ETEC): leading cause of traveler's diarrhea [39].
- enteroaggressive *E. coli* (EAEC): infections result in persistent, watery diarrhea and can cause outbreaks in developing countries [40].
- diffusely adherent *E. coli* (DAEC): cause of urinary tract infections, pregnancy complications, and diarrhea in children [41].
- enteroinvasive *E. coli*, including *Shigella* strains (EIEC): can cause dysentery [42].

In just the past three years, the CDC has reported five separate outbreaks of foodborne illness caused by the Shiga toxin-producing *E. coli* strain O157:H7 [43]. In total, these outbreaks led to 285 infections, 39 developments of HUS, and 6 deaths across the US (Arkansas, California, Minnesota, and New York) and still other cases in Canada [43]. The sources of the pathogen included leafy greens, romaine lettuce, alfalfa sprouts, ground beef, and soy nut butter products [43]. The elderly and young people are most likely to develop infections and suffer more severe complications [44]. In the case of the soy nut butter products, 81% of those infected persons were below the age of 18 [43].

Fortunately, these pathogens were not reported to have shown resistance to commonly used antibiotics. However, *E. coli* infections in healthcare settings prove much more difficult to treat. Carbapenem-resistant Enterobacteriaceae (CRE), of which approximately 1400 *E. coli* strains are members, are considered an urgent threat by the CDC [45]. There is little that can be done in the case of CREs by way of antibiotics as carbapenems are "the last line of defense" for multidrug-resistant bacterial infections [45]. Each year CREs cause around 9000 infections and 600 deaths in the US [45]. The prevalence of these pathogens is far-reaching; the CDC recorded at least one type of CRE in healthcare facilities in each of 44 states [45]. Pathogenic *E. coli* also present a serious threat, according to the CDC, in the form of extended spectrum β-lactamase (ESBL) producing Enterobacteriaceae [45]. ESBLs confer resistance to many common antibiotics such as penicillins and cephalosporins [45].

These drug-resistant strains cause 26,000 infections per year, result in 1700 deaths, and can cost infected individuals upwards of $40,000 in medical bills [45]. Presence of ESBL-production ability increases mortality rates due to Enterobacteriaceae infection by 57% for patients with bloodstream infections [45].

1.3.2 Motility and Chemotaxis

Peritrichous bacteria, like *E. coli*, navigate their environment by rotating multiple helical-shaped flagella counter-clockwise (CCW) and clockwise (CW) [46–48]. When rotating CCW the flagella bundle up to form a propeller, and when one or more flagella rotate CW the bundle comes undone and the cell spins randomly in place [46–48]. These rotation modes result in running (straight-swimming) and tumbling (reorientation) events, respectively [46–48]. In the absence of chemoattractant gradients this behavior causes a bacterium to perform a random walk [46]. In the presence of a chemical gradient the cell is able to traverse up or down that gradient (depending on the gradient content) by also employing its adaptive chemotactic signalling pathway [46].

The *E. coli* flagellum consists of three core parts: the basal body, the hook, and the filament [46–48]. The basal body is comprised of multiple macromolecular rings:

- C ring: the cytoplasmic ring formed by proteins FliG, FliM, FliN
- MS ring: membrane/supramembrane ring of FliF
- P ring: peptidoglycan ring
- L ring: lipopolysaccharide ring

[46–48]. The MS-C ring complex, as shown in figure 1, forms the motor that provides the necessary rotation for the run-tumble states [46–48]. The motor in *E. coli* is a H^+ driven stator-rotor motor in which approximately a dozen stators surround the inner rotor [46]. The stators are comprised of proteins MotA and MotB and attach to the peptidoglycan (PG) layer [46–48]. Protons crossing the cytoplasmic membrane provide the energy for motor rotation [46–48]. The motor then turns the flagellar hook, a joint made from FlgE

protein [46–48]. This hook rotates the filament, a long, helical FliC polymer measuring around 11 μm.

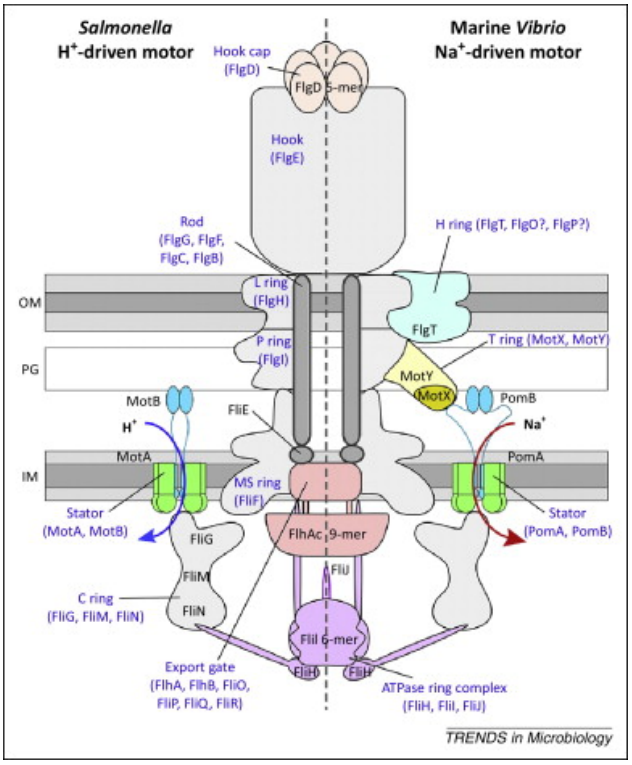

Figure 1: Structure of the flagellar motor and MS-C ring complex. Figure pulled from [47].

To reverse the direction of the motor, the phosphorylated chemotaxis protein CheY-P binds with FliM and FliN on the basal body [46–48]. This causes a conformational change in the FliG ring that results in CW rotation [47]. This interaction is mediated by the chemotactic signalling network of proteins. Trans-membrane chemoreceptors sense extracellular concentrations of attractants (such as serine and glucose) as well as repellents (such as fatty acids and alcohols) [46]. These receptors form a ternary complex with the autokinase CheA which is responsible for phosphorylating both CheY and CheB [46]. CheY and CheB, when phosphorylated, increase tumble frequency and update the adaptive sensory complex, respectively [46]. Under isotropic and homogeneous conditions, the phosphorylation rates of CheA will play out in a baseline manner causing sporadic tumbling [46]. When traveling in a favorable direction (such as up an attractant gradient), CheA auto-phosphorylation rates will

decrease with the goal of lowering the chances of tumbling [46]. Also, CheB demethylation of the adaptive feedback circuit will decrease, thus eventually returning the cell behavior to its baseline, even if a new higher concentration space is found [46]. In unfavorable or non-optimal directions, the previously experienced concentrations (as "remembered" by the feedback circuit) will promote auto-phosphorylation of CheA, thus increasing the phosphorylation rates of CheY and CheB [46]. These interactions will lead to increased tumble likelihood as well as demethylation of the glutamyl residues of the adaptive sensory complex, respectively [46]. The result for a cell in a chemoattractant gradient will thus be a biased random walk.

By allowing bacteria to optimize their motion, motility and chemotaxis play a crucial role in cell survivability and proliferation. Beyond this, flagella and motility also promote pathogenic virulence [49]. For *E. coli*, motility provides support in the initial phases of infection by offering the flagella as an adhesive with which to bind to surfaces and begin colonization [49]. Non-motile species, while still virulent, have a reduced infectious ability [49].

1.3.3 Mechanics of the *E. coli* Flagellar Motor

The *E. coli* flagellar motor is driven by proton flux across the cell membrane, not ATP hydrolysis as shown in the literature [48, 50]. The concentration difference of ions across the cytoplasmic membrane causes a voltage to arise [48, 50]. As ions travel down this electrochemical gradient they pass through the MotA/B stator proteins causing them to step along the rotor leading to rotation by generating torque [50].

The motor, attached to a left-handed helical flagellar filament by the hook, leads to propulsion as it rotates. *E. coli* cells possess multiple of these flagella that, when all rotating CCW, will bundle together to form a propeller [51]. Occasionally, as dictated by the internal chemotactic system, the flagella will reverse direction [48, 50, 51]. When even a single flagella reverses direction, the bundle will become undone and the cell will enter a tumbling state [48,

51]. In this tumbling state the normally left-handed helical filaments will reverse handedness [48, 50, 51]. This causes the cell to reorient itself randomly in-place. After a short duration, the default CCW rotation behavior will return, the bundle will re-form, and the cell will begin swimming again [48, 51]. This two-state switching behavior combined with the chemotactic signal transduction gives a cell the ability to swim in an optimal fashion in its environment.

2 Methods and Materials

2.1 *E. coli* Strain and Cell Growth

A K12 *E. coli* strain with a chromosomal *hns* gene knockout was used in this research. This strain was transformed with a plasmid coding for H-NS fused with the mEos3.2 fluorescent protein as well as resistance to antibiotics kanamycin and chloramphenicol. The strain is referred to as K12Δhns/pHNS-mEos3.2c1. This strain has been used in other studies from Dr. Yong Wang's lab investigating the antibacterial activities of Ag^+ and AgNPs.

For each experiment, a single K12Δhns/pHNS-mEos3.2c1 colony from an agar culture plate was inoculated in 5mL Luria Broth (LB) supplemented with the appropriate concentrations of kanamycin and chloramphenicol to select for the strain (50 μg/mL and 34 μg/mL, respectively). The culture tube was placed in a shaking incubator (37° C, 250 RPM) and grown overnight. The next day, the OD_{600} (optical density at 600nm) was measured (Implen NanoPhotometer). The liquid culture was then diluted 5000:1 in 5mL of fresh LB with antibiotics. This new culture tube was then regrown at 32° C and 250 RPM. When the culture had regrown to mid-exponential phase ($OD_{600} \approx 0.3$), the first set of images was taken.

2.2 Phase-Contrast Microscopy

Bacteria were imaged at room temperature using an Olympus IX-73 inverted microscope with a 100X, NA=1.25 phase-contrast, oil-immersion objective. Movies were acquired with an EMCCD camera (Andor Technology) and the specifications were controlled using Micro-Manager.

Unlike other means of microscopy, like brightfield, which solely use changes in transmitted light intensity to create an image, phase-contrast microscopy takes advantage of the fact that light passing through a transparent object, such as an *E. coli* cell, will undergo a phase shift as well as an intensity change [52]. This phase shift, although slight, can be used to distinguish a sample from its background (so long as there is a change in index of refraction) [52].

Brightfield microscopy typically fails to produce high contrast images for transparent, thin samples because the change in intensity alone is small [52].

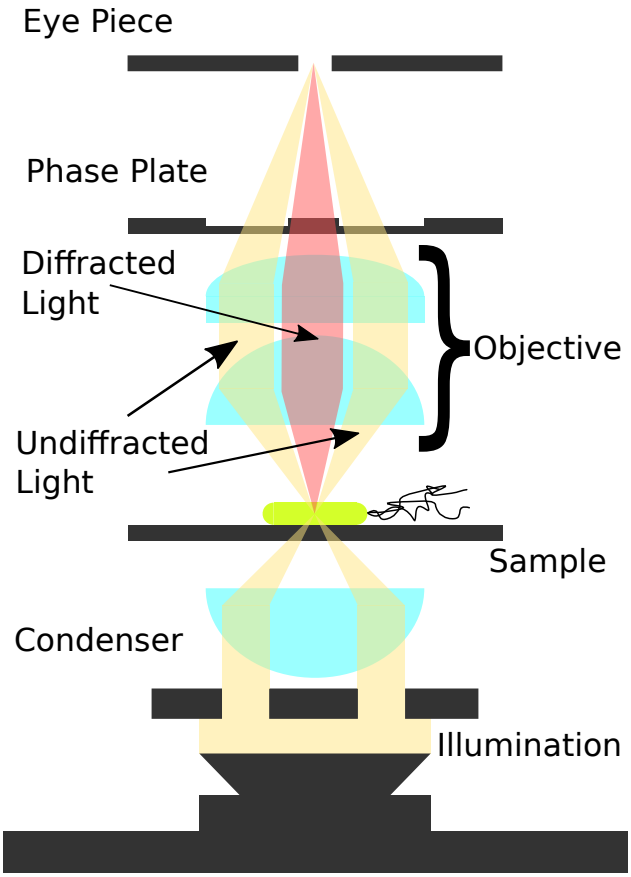

Figure 2: Cross-section of a phase-contrast microscope schematic [52, 53]. Light diffracted by the cells (red) passes through the phase plate un-delayed. The light which passes through the sample un-diffracted (yellow) is phase-delayed by $\pi/2$. The two beams recombine at the eye piece to form an image.

Phase-contrast microscopy attains higher contrast by phase-delaying the un-diffracted light passing around the sample, and recombining that light with the sample-diffracted light. As depicted in figure 2, light is passed through an annular diaphragm and focused on the sample using a condenser. Light diffracted by *E. coli* cells passes on to the objective along with the un-diffracted light where both are collected onto the back focal plane of the objective. The back focal plane is equipped with an annular phase plate where the un-diffracted light passes through a region with a smaller optical path length (OPL) than the the region for the diffracted light. This causes the phase of the un-diffracted light to be delayed (typically

by either $\pi/2$ or $3\pi/2$ radians), thus amplifying the phase change caused by the transparent sample [52]. Without this delay the contrast between diffracted and un-diffracted light would be too poor.

To calculate the image intensity we first look to the amplitude transmission of the transparent sample, t, given by

$$t(x,y) = \mathrm{e}^{i(\phi(x,y)-\bar{\phi})} \tag{1}$$

where $\bar{\phi}$ is the average phase of the un-diffracted light and $\phi(x,y)$ is the phase of the diffracted light at a point (x,y) on the sample [52]. The phase shift, $(\phi(x,y)-\bar{\phi})$ will be very small so the approximation

$$t(x,y) = \mathrm{e}^{i(\phi(x,y)-\bar{\phi})} \approx 1 + i(\phi(x,y)-\bar{\phi}) \tag{2}$$

can be made [52]. In this Taylor series expansion, the real term represents the un-diffracted light and the imaginary term represents the light diffracted due to the *E. coli* cell [52]. The image produced by this effect, without the phase plate, will then be

$$I(x,y) = |t(x,y)|^2 = \left|1 + i(\phi(x,y)-\bar{\phi})\right|^2 = 1 \tag{3}$$

[52]. This illustrates the difficulty that brightfield microscopy techniques face when trying to image thin, transparent samples; the image will have almost no contrast. With the addition of a phase plate, however, the phase change becomes more apparent. If the phase plate delays the phase of the un-diffracted light (the unity term in equation 2) by $\pi/2$ radians then t becomes

$$t(x,y) = \mathrm{e}^{-i\frac{\pi}{2}} + i(\phi(x,y)-\bar{\phi}) = i(\phi(x,y)-\bar{\phi}-1) \tag{4}$$

[52]. Thus, the image intensity becomes

$$I(x,y) = \left|i(\phi(x,y)-\bar{\phi}-1)\right|^2 \approx (1+2\bar{\phi}) - 2\phi(x,y) \tag{5}$$

[52]. Therefore, the image intensity at each point (x, y) will be linearly proportional to the phase change at that point [52]. Light passing through an *E. coli* cell will have a markedly lower brightness than the unimpeded light surrounding the cell. This results in the cells appearing black against a white background. This is positive phase-contrast imaging and will be used in this work [52]. In a similar regime, the phase delay can be set to $3\pi/2$ rather than $\pi/2$. This causes the cells to appear white on a black background [52]. This is negative phase-contrast imaging [52].

2.3 Preparation of Silver Nitrate Solution

Silver solution stock was made by dissolving 99.9%+ pure $AgNO_3$ in sterile, deionized water to a final concentration of 10mM. The concentrations used in this set of experiments were 30 and 40 μM Ag^+. These were selected so as to not completely inhibit the growth of *E. coli*. Previous research found that around 60 μM Ag^+ caused total inhibition of bacterial growth [54]. Therefore, I chose to use two concentrations close to the same concentrations used in [54] that were found to not completely stop cell growth.

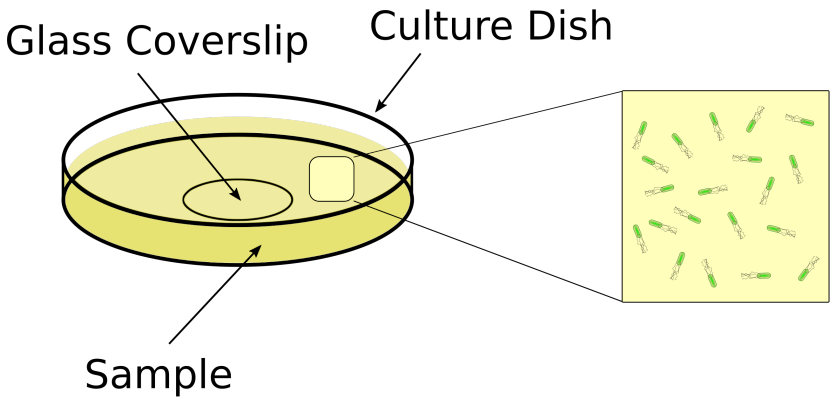

Figure 3: Cartoon of culture dish setup for free-swimming experiments.

2.4 Free-Swimming Experiments

In this set of experiments, *E. coli* cells were allowed to swim freely in the presence of silver ions in a 35 mm culture dish with a glass coverslip bottom, as depicted in figure 3. Before imaging, culture dishes were serially washed with soap & water, sodium hydroxide, and 190 proof ethanol for 30 minutes each step. Dishes were rinsed thoroughly with deionized water between steps. Culture dishes were then air-dried and 200 μL of 1% BSA (bovine serum albumin, Biotechnology) was added to the culture dish and let incubate for five minutes. Afterwards, excess BSA was removed and washed off using 1X PBS.

Once the liquid bacterial culture reached mid-log phase, 2mL was taken from one of the samples and added to the dish. The sample was allowed to adjust to the environment and room temperature for fifteen minutes. The remaining samples were inoculated with either 30 or 40 μM Ag^+ (or 0 μM Ag^+ for negative control experiments) and placed back in the shaking incubator. Again 1, 2, 4, and 8 hours post initial imaging time, a sample was imaged on the culture dish. If, however, the OD_{600} was too high for adequate imaging (typically no more than 0.6), then the sample was diluted to OD_{600}=0.3 in LB with antibiotics and the appropriate amount of Ag^+ for that experiment. Each time, the total volume in the dish was 2mL.

2.4.1 Acquisition Protocol

Movies of the 512x512 region of interest were acquired at 18.4 frames per second (fps) and saved to TIFF files. Pixel size was calculated to be 160nm, thus ROI size was approximately 82x82 μm. For each imaging time (0, 1, 2, 4, 8 hours from silver inoculation), five movies of 5000 frames were taken. Each movie captured a different region of the coverslip. Experiments were repeated once on a separate day for each nonzero concentration of Ag^+. Data from the repeats were aggregated together appropriately.

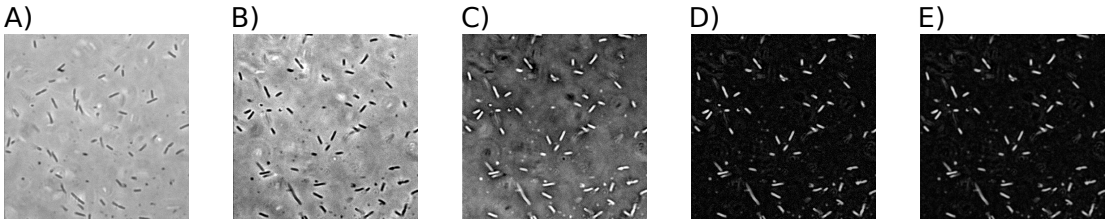

Figure 4: Image processing steps performed in ImageJ for swimming experiments. A) Raw image data. B) Image with reset minimum and maximum intensities. C) Inverted image. D) Image with subtracted background (rolling ball radius=10px). E) Final smoothed image.

2.4.2 Image Processing Steps for Swimming Experiments

Movies were processed in ImageJ (NIH) by first converting to 8-bit, inverting the intensity, resetting the minimum and maximum intensity values, smoothing, and finally subtracting the background using the rolling ball method with a radius of ten pixels. The cleaning steps performed are illustrated in figure 4. After cleaning, movies were ran through a series of MATLAB scripts developed by my advisor, Dr. Yong Wang. These scripts first detected the bacteria in frame, then culled erroneous detections based on morphology (area, length, width, others), and finally strung detections together into tracks.

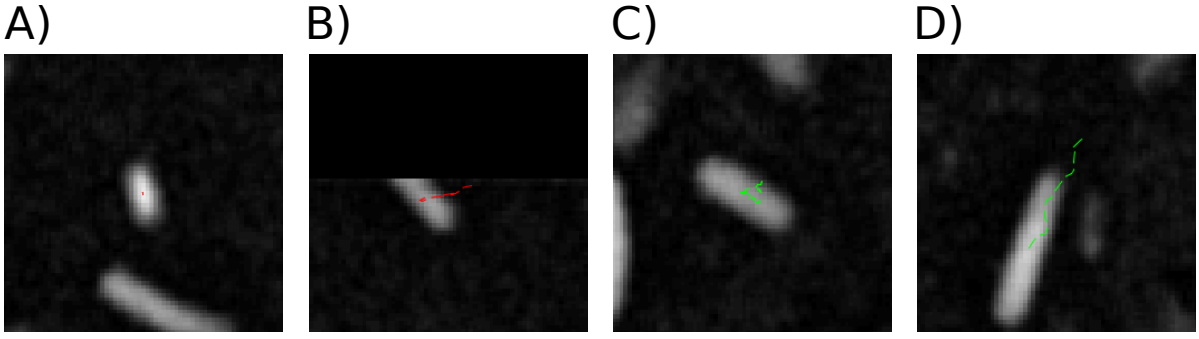

Figure 5: Examples of rejected and accepted tracks. A) Cell is completely immobile and for that reason it is rejected. B) A substantial portion of the cell is outside the ROI and thus the track produced does not accurately capture all of the cell's motion. C) This cell is not swimming but rather appears to be diffusing; this track is accepted. D) cell swims in roughly a straight path, so it is accepted.

2.4.3 Track Selection

The resulting tracks after processing were manually selected for usability. Tracks were removed from further analysis if the cell was completely stationary, if the cell was part of a larger cluster, or if the track was not representative of the actual motion. A few exemplary tracks and their corresponding labels as color are shown in figure 5.

The remaining, selected tracks were kept for further analysis. Each imaging time has with it around 300 - 500 selected tracks of varying length.

2.4.4 Motility as Quantified by Swimming Velocity

In a homogeneous and isotropic environment, *E. coli* swim in a run and tumble in which long swimming periods are interrupted by relatively short reorientation periods [55]. Closer to surfaces, however, bacteria will move in right-handed circular patterns and display longer run times [56]. In either regime, *E. coli* bacteria can swim at speeds up to 30 μm/s, up to 15 times their cell length [55]. Using the selected track data, I found the swimming velocity of each cell at frame t by simply using equation 6 where fps is the frames per second of the imaging session.

$$v_t = \frac{\Delta r}{\Delta t} = \sqrt{(x_t - x_{t-1})^2 + (y_t - y_{t-1})^2} \times \text{fps} \tag{6}$$

2.4.5 Chord-Arc Ratio as a Measure of Tortuosity

As *E. coli* bacteria swim in their containing media they alternate between running and tumbling steps. During tumbling times, the flagellar bundle comes undone and the cell randomly reorients its swimming direction. Tortuosity, in general, is a property of a path between two points being curved. Tortuosity has been used as a feature of interest in a variety of scientific domains including medicine, ecology, and geology [57–59]. While each of these disciplines vary in their exact definition of tortuosity or means of calculating it, tortuosity can broadly be calculated as the ratio between displacement and total distance traveled. For this research, a modified version of the arc-chord ratio (ACR) used by Pottash

et al. is employed [60]. We will define the chord-arc ratio (CAR) as

$$CAR = \frac{\max_{i,j} |\vec{r}_i - \vec{r}_j|}{\sum_{k=1}^{N-1} |\vec{r}_{k+1} - \vec{r}_k|} \tag{7}$$

where $\vec{r}$ is the position vector and N is the number of frames of the trajectory. This value will range from 0 to 1 corresponding to exclusive tumbling and straight line trajectories, respectively. The population distribution of the CAR values within a sample provides a metric with which to compare swimming tortuosity over time as well as between experiments with different concentrations of silver ions.

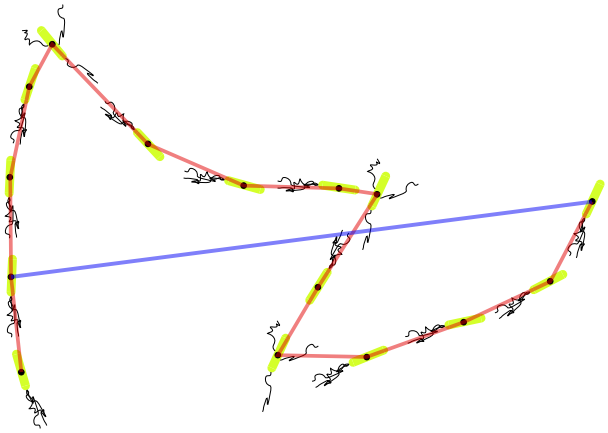

Figure 6: An example path traveled by a swimming *E. coli* cell. The chord-arc ratio is defined as the total path length (red segments) divided by the longest distance between any two points on the path (blue line).

2.4.6 Swimming Behavior Modeled with Anomalous Diffusion Relation

Although diffusion analysis is typically reserved for investigating the motion of individual molecules, in this research I have used it as a value to determine the viability of a cell after treatment with silver ions. The Einstein relation, used to model a random walk such as that seen with Brownian motion, is

$$\langle (\Delta r)^2 \rangle = 2dD\tau \tag{8}$$

where d is the number of dimensions of freedom, D is the diffusion coefficient, and τ is the lag-time. For this research, I used $d = 2$ since the bacterial tracks exist in just the plane of the ROI.

Swimming bacteria will not, however, follow a random walk when close to a surface such as a coverslip [56]. Therefore, I will use the anomalous diffusion equation which generalizes equation 8 to include superdiffusion and subdiffusion modes of movement.

$$\langle(\Delta r)^2\rangle = 4D\tau^{\alpha} \tag{9}$$

or

$$\log\langle(\Delta r)^2\rangle = \alpha \log\tau + \log 4D \tag{10}$$

As seen in equation 9, the relationship between mean square displacement (MSD) and τ is a power law rather than linear. When $\alpha > 1$ motion is superdiffusive (also called ballistic), and when $\alpha < 1$ motion is subdiffusive. Cells able to propel themselves will likely be superdiffusive.

In analyzing the bacterial tracks, I used the numpy and scipy packages from Python to fit MSD vs τ data to equations 9 and 10 and extract D and α values for different imaging times and concentrations of $AgNO_3$ [61].

2.5 Tethering Assay Experiments

In this set of experiments, cells were tethered to the glass coverslip of the culture dish using a FliC antibody, as depicted in figure 7. Using this assay, rotation of the flagella which would otherwise have caused propulsion instead caused rotation of the cell body parallel to the coverslip. Clean culture dishes were prepared with a serial treatment of biotinylated-BSA (200 μL, 1 mg/mL), neutravidin (200 μL, 0.5 mg/mL), and FliC antibody (400 μL, 0.25 μg/mL) with 1X PBS washing steps in-between. Similar to the swimming experiments, 2mL of *E. coli* sample was added to the prepared dish once $OD_{600}\approx 0.3$. However, in order

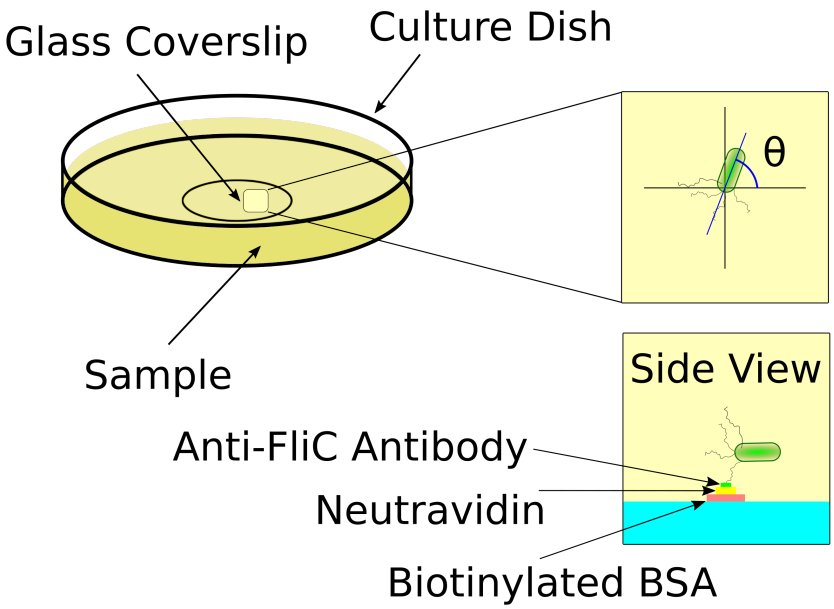

Figure 7: Cartoon of culture dish setup for tethering assay experiments.

to isolate just those cells stuck to the coverslip, cells that remained unstuck were removed via washing away the excess LB media and replacing it with fresh LB and antibiotics.

2.5.1 Acquisition Protocol

To maximize temporal resolution, the ROI was cropped to 64x64 pixels (10.24 μm x10.24 μm) around an individual tethered cell. Exposure time was 5ms. Frame-rate for each move was 71 fps. After acquiring 10,000 frames of silver-free tethered behavior, Ag^+ was added directly to the culture dish such that the final concentration was 40 μM. Images of the same cell were then recorded for 100,000 more frames as Ag^+ dispersed throughout the media. In total, data from 17 cells were captured in this way from experiments on different days. In addition, data from 10 cells not treated with silver were acquired.

2.5.2 Image Processing Steps for Tethering Assay Experiments

Cells were detected and characterized using the regionprops function from the Python scikit-image package. In order to analyze only one cell per frame, regions (sections of 1's in the

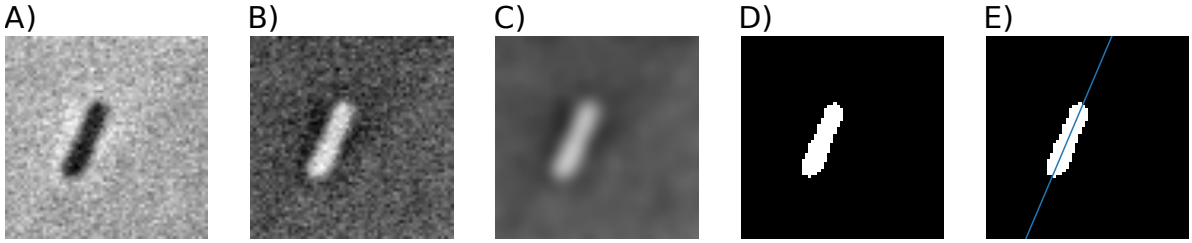

Figure 8: Image processing steps performed in ImageJ and Python for tethering experiments. A) Raw image data. B) Inverted image. C) Gaussian blurred image (radius=2 in ImageJ). D) Thresheld image using the intermodes method available with ImageJ. E) Binary mask with line indicating the primary axis angle calculated by the regionprops function from Python's scikit-image library (from the 'measure' module).

binary mask) were thresheld based on area, and further any frames with more than one region were removed from analysis. Primary axis angle of the cells was found and used to calculate the rotational velocity. This angle was found using the regionprops function from scikit-image [62]. The change in this angle, defined as ω, was calculated by finding the difference across a single frame, multiplying by the frame-rate, and correcting for any jumps caused by a switch from $\sim \pi$ to $\sim -\pi$ or vise versa.

2.5.3 Modeling Rotation Behavior as a Hidden Markov Process

A random variable in time X_t is said to follow to follow a Markov process (possess the Markov property) if the value of X at time step t is solely dependent on the value of that variable at the previous time step (X_{t-1}) [63]. This demands that, for every sequence $u_0, u_1, \ldots, u_{t-1}, u_t$ and $t \geq 1$

$$\Pr\{X_t = u_t | X_0 = u_0, X_1 = u_1, \ldots, X_{t-1} = u_{t-1}, X_t = u_t\} = \Pr\{X_t = u_t | X_{t-1} = u_{t-1}\}. \quad (11)$$

This Markov process (also called a Markov chain) can be encapsulated in a stochastic transition matrix A in which the transition probability from state i to state j is given by A_{ij}. These transitions are taken to occur between discrete time points. Additionally, a Markov

process has a stationary distribution π associated with it that will also determine the probability of a sequence starting in a particular state. π must be a vector whose components are non-negative and sum to 1. For time-homogeneous Markov chains, such as those used in this research π must be invariant under transformation with A (i.e. $\pi A = \pi$).

As an example, let's suppose we have determined that the weather on a given day in Fayetteville follows a Markov process with possible states sunny (S) and rainy (R) and transition matrix

$$A = \begin{array}{c} \\ S \\ R \end{array} \begin{array}{c} \begin{array}{cc} S & R \end{array} \\ \begin{bmatrix} 0.7 & 0.3 \\ 0.4 & 0.6 \end{bmatrix} \end{array}$$

(This model is adapted from [64]). As can be seen, the transition probability from a sunny

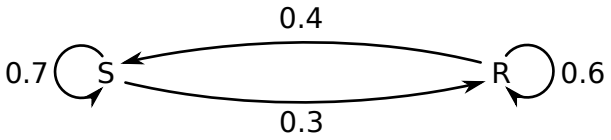

Figure 9: Graphical representation of weather transition matrix.

day to another sunny day is 0.7 and the probability from a sunny day to a rainy day is 0.3. The stochastic matrix can also be represented with a graph, as depicted in figure 9. The stationary distribution in this case will be given by

$$\begin{aligned} \pi A &= \pi \\ \begin{bmatrix} p & 1-p \end{bmatrix} \begin{bmatrix} 0.7 & 0.3 \\ 0.4 & 0.6 \end{bmatrix} &= \begin{bmatrix} p & 1-p \end{bmatrix} \\ \begin{bmatrix} 0.3p + 0.4 & -0.3p + 0.6 \end{bmatrix} &= \begin{bmatrix} p & 1-p \end{bmatrix} \\ p &= \frac{4}{7} \\ \Rightarrow \pi &= \begin{bmatrix} \frac{4}{7} & \frac{3}{7} \end{bmatrix}. \end{aligned}$$

The transition matrix can be used to calculate the likelihood of a given sequence of states being created by that Markov model. Suppose we were given a sequence

$$\mathbb{H} = S \to R \to R \to S \to R \to S$$

the likelihood of our model producing this state is the product of the probability of beginning in the initial state and the probabilities of making the transitions contained in the sequence. So,

$$\begin{aligned} L(\mathbb{H} = S \to R \to R \to S \to S \to S) &= \pi_S \times A_{SR} \times A_{RR} \times A_{RS} \times A_{SR} \times A_{RS} \\ &= \frac{4}{7} \times 0.3 \times 0.6 \times 0.4 \times 0.6 \times 0.4 \\ &= 0.00987 \quad . \end{aligned}$$

Succinctly, for a sequence $\mathbb{H}$ consisting of k time points with states $u_t \in \mathbb{M}$, the likelihood is

$$L(\mathbb{H}|A) = \pi_{u_1} \times \prod_{t=2}^{k} \Pr\{\mathbb{H}_t = u_t | \mathbb{H}_{t-1} = u_{t-1}\} = \pi_{u_1} \times \prod_{t=2}^{k} A_{u_{t-1}u_t} \tag{12}$$

[63]. Or, for convenience, we may calculate the negative log likelihood ℓ when working with long sequences (and thus low likelihoods).

$$\ell = -\ln(L) \tag{13}$$

[63]. The likelihood equation can be used to estimate the fitness of our transition matrix A when fitting a model, or to compare the chances of a model producing one sequence over another.

Many biological systems can be modeled as Markov processes including the proliferation of epithelial cells [65], and macromolecular sequence prediction in bioinformatics [66]. Many times in real applications, however, the states of the Markov process are not directly ob-

servable. Rather, the observed state Y_t is the emission of a random function on the now "hidden" state X_t. This scenario is described by a Hidden Markov model (HMM). For this mathematical model, in addition to the transition matrix A and the stationary distribution vector π there exists a stochastic emission matrix B that describes the output, Y_t, of the HMM based on the hidden state, X_t. The elements of B are defined as

$$B_{uv} = \Pr\{Y_t = v | X_t = u\}, \quad \forall u \in \mathbb{M}, \quad v \in \mathbb{N} \tag{14}$$

where $\mathbb{M}$ and $\mathbb{N}$ are the sets of possible hidden and output states, respectively [63].

In our Markov-ian weather example, if we are not able to directly view the state of the weather (maybe our problem involves determining the weather on days in the past), then $\mathbb{N}$ would represent the set of observable indicators for the hidden state (e.g. correlated features like temperature recordings). If we take $\mathbb{N}$ to contain states corresponding to warm days (W), temperate days (T), and cold days (C) then the emission matrix, B, is

$$B = \begin{bmatrix} \Pr\{Y_t = W | X_t = S\} & \Pr\{Y_t = T | X_t = S\} & \Pr\{Y_t = C | X_t = S\} \\ \Pr\{Y_t = W | X_t = R\} & \Pr\{Y_t = T | X_t = R\} & \Pr\{Y_t = C | X_t = R\} \end{bmatrix}$$

where the sum of each row should be 1. This example employs an HMM with multinomial (discrete) emissions. Emissions with continuous (e.g. Gaussian) distributions are entirely possible, and will be used in this research.

Now, rather than observing a sequence of states, we will work with a sequence of emissions, $\mathbb{E}$, and attempt to discern the most likely sequence of hidden states, $\mathbb{H}$. The Viterbi algorithm is a common tool for achieving this. To understand the utility of the Viterbi algorithm let's first implement a naive approach to find $\mathbb{H}$ given $\mathbb{E}$.

Let $\mathbb{E} = v_1 \to \cdots \to v_{n-1} \to v_n$ represent a sequence of k observed emissions. In order to find the most likely sequence, $\mathbb{H}$, of hidden states, u, we may try to find the probability of each sequence of hidden states of length k emitting the sequence given by $\mathbb{E}$. This involves

finding the maximum value among

$$\Pr\{\mathbb{H} = u_1 \to u_1 \to \cdots \to u_1 \to u_1 | \mathbb{E}\}$$
$$= (\pi_{u_1} \times B_{u_1,v_1}) \times (A_{u_1,u_1} \times B_{u_1,v_2}) \times \cdots \times (A_{u_1,u_1} \times B_{u_1,v_n})$$
$$\Pr\{\mathbb{H} = u_1 \to u_1 \to \cdots \to u_1 \to u_2 | \mathbb{E}\}$$
$$= (\pi_{u_1} \times B_{u_1,v_1}) \times (A_{u_1,u_1} \times B_{u_1,v_2}) \times \cdots \times (A_{u_1,u_2} \times B_{u_2,v_n})$$

$$\cdots$$

$$\Pr\{\mathbb{H} = u_n \to u_n \to \cdots \to u_n \to u_n | \mathbb{E}\}$$
$$= (\pi_{u_n} \times B_{u_n,v_n}) \times (A_{u_n,u_n} \times B_{u_n,v_n}) \times \cdots \times (A_{u_n,u_n} \times B_{u_n,v_n})$$

Computationally, this is very expensive as it requires finding the probability for each of the m^k possible sequences, where m is the cardinality of $\mathbb{M}$. The Viterbi algorithm makes use of the fact that, when constructing the hidden sequence $\mathbb{H}$, choosing the most probable subsequent state at any intermediate time point will lead to the most probable sequence. The task of finding $\mathbb{H}$ becomes one solved quickly with dynamic programming. An implementation in Python 3 is shown on the next page.

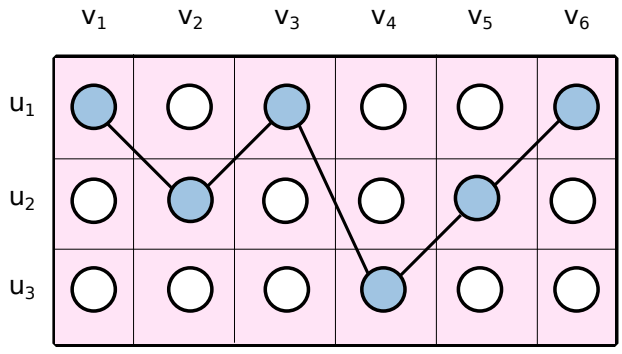

Figure 10: A simple illustration of the path that would be found using the Viterbi algorithm.

```
def argmax(seq):
  index, maximum = 0, seq[0]
  for i, value in enumerate(seq[1:]):
      if value > maximum:
          index, maximum = i + 1, value
  return index

def viterbi(TRANSMAT, EMAT, H_STATES,
            OB_STATES, OB_SEQUENCE, STAT_DIST):
  """
  TRANSMAT    : (m x m) trans. matrix | EMAT: (m x n) emission matrix
  H_STATES    : m hidden states       | OB_STATES: n observable states
  OB_SEQUENCE : array of observations | STAT_DIST: stationary dist.
  """
  h_sequence = list()
  for i, ob_state in enumerate(OB_SEQUENCE):
      if i == 0:  # Find the first hidden state
          ob_index = OB_STATES.index(ob_state)
          h_index = argmax([
              STAT_DIST[j] * EMAT[j][ob_index]
              for j in range(len(H_STATES))
          ])
          h_sequence.append(H_STATES[h_index])
      else:  # Find the next hidden state
          ob_index = OB_STATES.index(ob_state)
          prev_h_index = H_STATES.index(h_sequence[-1])
          h_index = argmax([
              TRANSMAT[prev_h_index][j] * EMAT[j][ob_index]
              for j in range(len(H_STATES))
          ])
          h_sequence.append(H_STATES[h_index])
  return h_sequence
```

Visually, the Viterbi algorithm can be understood as a path-finding algorithm where we progress from a state to the next by maximizing the probability. A simple diagram with $m = 3$ and $k = 6$ is shown in figure 10.

Returning to our example model, if the emission matrix is

$$B = \begin{array}{c} \\ S \\ R \end{array} \begin{array}{c} \begin{array}{ccc} W & T & C \end{array} \\ \begin{bmatrix} 0.5 & 0.4 & 0.1 \\ 0.1 & 0.2 & 0.7 \end{bmatrix} \end{array}$$

then our graph has a hidden layer that we cannot directly observe, as indicated by the

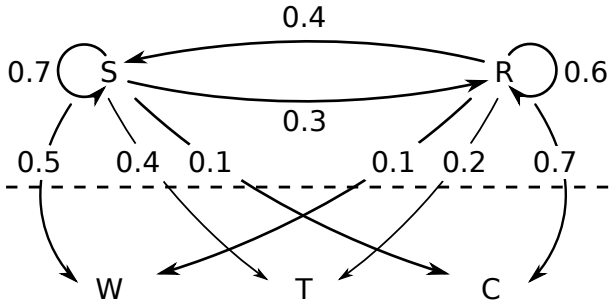

Figure 11: The full hidden Markov model including emission probabilities. The hidden states are not directly visible rather only the emissions are observable (lower nodes).

dashed line in figure 11.

If we observe a state sequence given by

$$\mathbb{E} = C \to C \to T \to W \to T \to C \to W \to C \to T \to C \to C$$

then we can use the Viterbi algorithm and find

$$\mathbb{H} = R \to R \to S \to S \to S \to R \to S \to R \to S \to R \to R$$

In this research, I fit the switching behavior between running and tumbling modes of

the *E. coli* flagellum to a two-component hidden Markov model with Gaussian emission distributions. The observable, in this case, was the rotational velocity ω of the cell when tethered to a glass coverslip. The HMM contains the mean ω and standard deviation for the emissions of each hidden state. To implement the modeling, I used the open source hmmlearn library available in Python [67]. This library handles fitting the model, calculating the stationary distributions, means, standard deviations, as well as the Viterbi algorithm for predicting the hidden states of a given sequence of ω.

3 Results and Discussion

3.1 Free-Swimming Experiments

3.1.1 Optical Densities Confirm Silver Ions Suppress Growth of *E. coli*

The optical density at 600 nanometers (OD_{600}) is commonly used to measure density of bacterial cultures. Uninterrupted, the OD_{600} of a bacterial culture will follow a logistic growth curve consisting of the lag phase, exponential growth phase, and steady state phase as the culture reaches its carrying capacity. Figure 12 shows the culmination of the OD_{600} values measured during each of the different swimming experiments. The data shown in figure 12, listed in table 1, is the average OD_{600} with the standard error at each time point segregated by the Ag^+ concentration used. Silver ions were added at the 0 hour point (once $OD_{600} \approx 0.3$).

OD_{600}						
	0 μM Ag^+		30 μM Ag^+		40 μM Ag^+	
Time (Hours)	Mean	SEM	Mean	SEM	Mean	SEM
-1	0.141	0.006	0.122	0.003	0.152	0.010
0	0.360	0.014	0.295	0.007	0.400	0.015
1	0.664	0.010	0.324	0.008	0.418	0.021
2	0.984	0.039	0.332	0.010	0.417	0.023
4	1.400	0.062	0.319	0.019	0.437	0.030
8	1.731	0.022	0.289	0.046	0.451	0.048

Table 1: OD_{600} data from swimming experiments at different concentrations of Ag^+. Mean and standard error of the mean are shown here for 0, 30, and 40 μM Ag^+.

The 0 μM Ag^+ (control) curve follows the expected sigmoid shape. The silver-treated samples experience lag time extension and no longer grow exponentially. These results match those found by research done in Dr. Wang's lab [54]. We see that after 8 hours there is an 83% decrease in mean OD_{600} for 30 μM Ag^+ and a 73% decrease for 40 μM Ag^+. Additionally, while the control culture underwent an almost 5-fold increase in mean OD_{600} the silver-treated samples decreased by 2% and increased by 12% for 30 and 40 μM Ag^+, respectively.

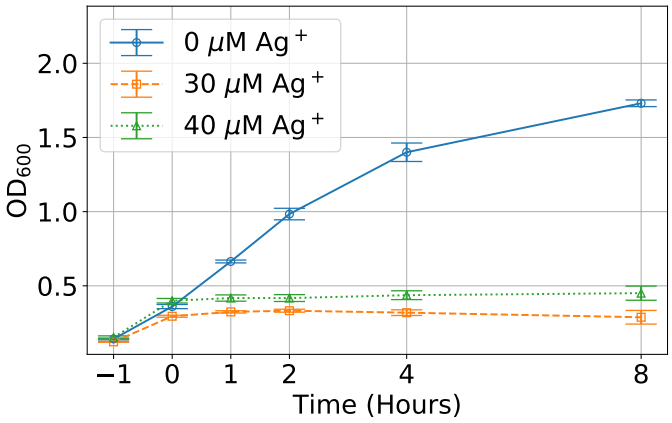

Figure 12: Optical density at 600nm plotted versus imaging time, averaged for each experiment. Error bars display the standard error of the mean. Silver was added after the 0 hour images had been taken. OD_{600} was approximately 0.3 at the start of imaging for each experiment. The 0 μM Ag^+ samples showed the expected logistic growth behavior. Silver-treated samples ceased their exponential growth.

3.1.2 Silver Ions Cause a Temporary Decrease in Swimming Velocity and Increase in Path Tortuosity

Using phase-contrast microscopy and computer vision techniques I was able to track individual *E. coli* cells as they swam in LB media. These tracks, as shown in figure 13 extended about 20 microns over the course of approximately six tenths of a second when not treated with silver. This quick speed is, however, not retained by most cells after silver ions have been introduced into the media. As shown in the middle and bottom rows of figure 13, the majority of the tracks appeared much shorter just after silver ions were added. Rather than swimming in straight yet slightly curved paths, their behavior was a mix of this original type of motion as well as what appears to be simple diffusion. I will show in the next section that the cells were, however, mostly superdiffusive.

Additionally, although the growth of the bacterial culture did not appear to make any sort of recovery, the swimming behavior of many cells reverted to that of the control. Nonetheless, many silver-treated cells in the ROI at later times were not swimming with much directed motion. To further visualize the inability of silver-treated *E. coli* to propel themselves as

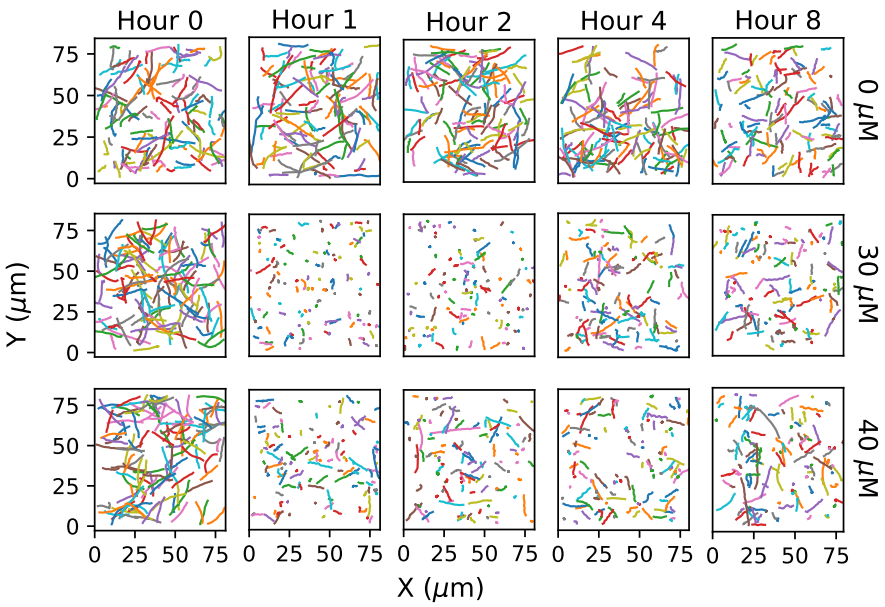

Figure 13: A subsample of the thousands of selected tracks are drawn from each hour and concentration. The number of frames for each track is held constant so as to prevent bias based on length. Upon silver entering the bacterial media (hour 1) the cells' trajectories become much shorter. As time since addition of $AgNO_3$ increases some tracks look reminiscent of their control counterparts.

efficiently, I repositioned each of the trajectories to begin at the same origin to create a "firework" plot (also called a rose plot by [60]). From this plot, as shown in figure 14, the different displacement capabilities based on concentration and time since treatment are more readily apparent. I found the displacement of the 50^{th} and 75^{th} percentile cell and over-layed those values as solid and dashed circles, respectively.

For the control swimming experiment the swimming capability stayed relatively constant, as seen with the percentile circles. However, at hour 8, both the 50^{th} and 75^{th} percentile radii decreased. This sudden decrease in swimming ability was likely due to the high OD_{600} at that time ($\sim$1.7). At this high of density, the culture became much more crowded. In this situation nutrients such as carbon, nitrogen, phosphate, sulfur, and necessary ions become more scarce [68]. As a reaction to this starvation, *E. coli* and other bacteria may relinquish some cellular functions, including motility and flagella synthesis, in order to cope [68]. More investigation would be needed to ascertain whether the observed change in swimming ability

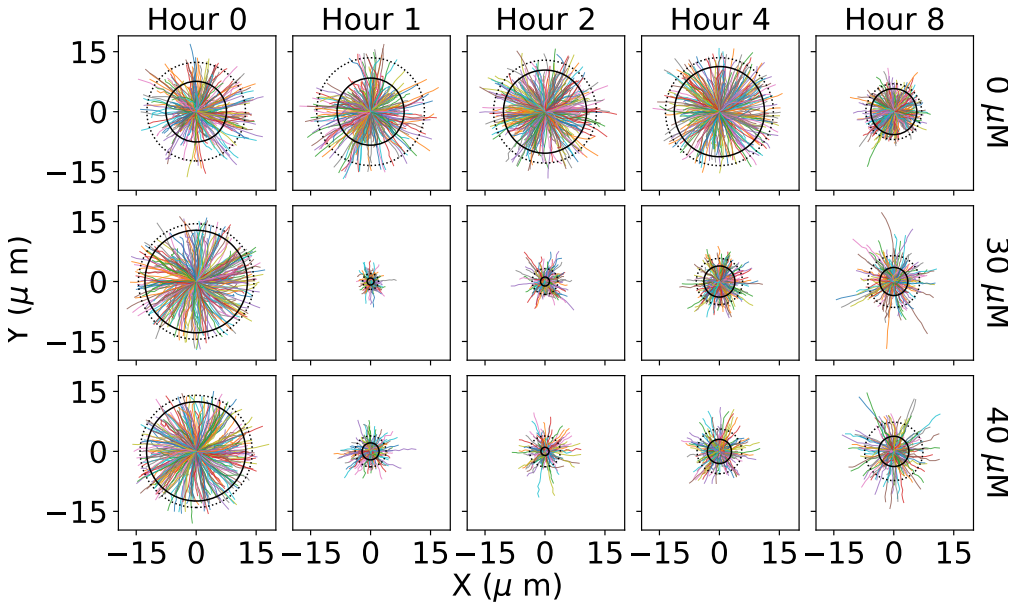

Figure 14: Here, trajectories from figure 13 are reoriented to begin at the origin. The solid and dashed circles represent the 50$^{\text{th}}$ and 75$^{\text{th}}$ percentiles of cells' total "radial" displacement. From the changing radii of the percentiles as time increase it is clear, at least visually, that silver affects the swimming behavior of bacteria in such a way that they are not able to travel as far of distances given the same amount of time.

here was directly due to a lack of the necessary cellular components.

From these trajectories, the swimming velocities was easily obtained. The distributions of velocities at each time point are plotted in figure 15. I constructed these distributions by creating individual velocity histograms with 25 bins between 0 and 35 μm/s. These histograms were then averaged over for each hour and concentration, appropriately. The error bars in the figure show standard error of the mean for each bin. Finally, for easy comparison, the maximum of each curve was reset to unity. The first 5 figures show the distributions for each concentration at each of the 5 imaging times. The lower right sub-figure displays the mean and standard error obtained from all of the data aggregated.

One hour after silver was added to the media, both the 30 and 40 μM Ag^+ distributions showed a strong decrease in the value of the bin corresponding to the mode. The mean value decreased below 5 μm/s after 1 hour and steadily increased back to almost 10 μm/s after 8 hours. The control data showed an increasing mean velocity until the 8 hour mark when the

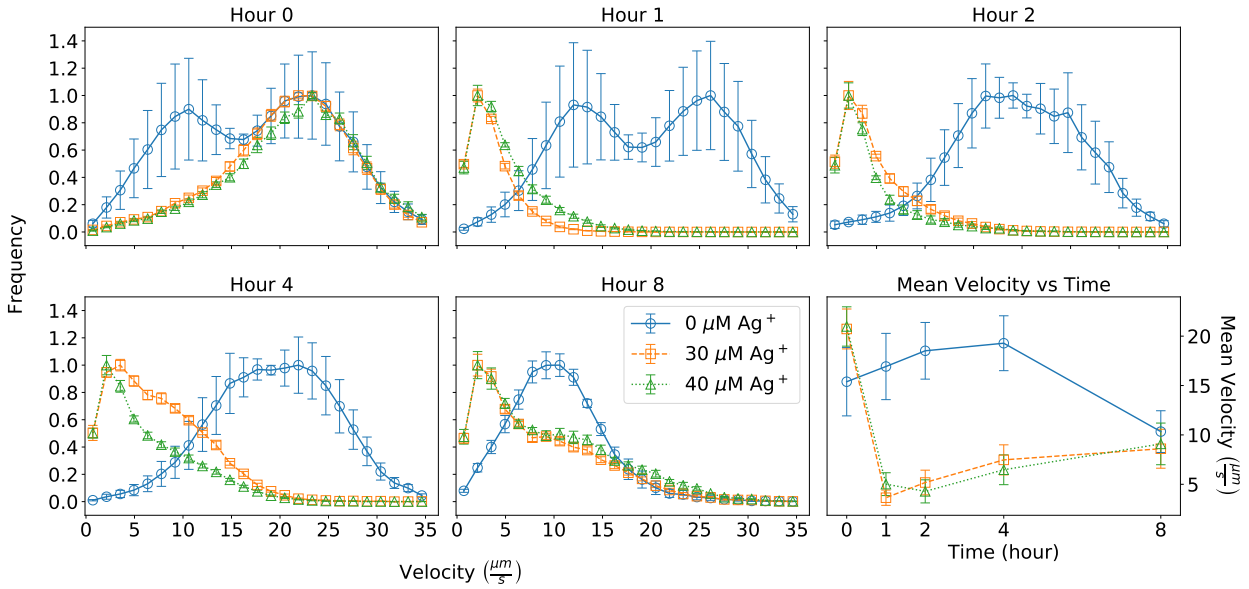

Figure 15: Velocity histograms for each movie were made and then averaged over according to Ag^+ concentration and time to create the above histograms. Data is split into 25 equally sized bins. The error bars represent the standard error of the mean for each bin. The mean velocity over time (lower right) supports the qualitative result from the firework plot (figure 14); the mean velocity immediately decreases after silver is added. This velocity slowly increases over time. The value of the control mean velocity is not constant in time, interestingly. The velocity increases slightly to a maximum around 20 μm/s at 4 hours post-addition of Ag^+ until falling at hour 8.

velocity dropped down to almost meet the mean velocity value for the silver-treated cells.

The observed change in velocity could be directly caused by one of many phenomena. It is possible that the silver ion concentration was high enough in the solution to kill the bacteria; this would clearly decrease the swimming velocity. It is also possible that silver ions were directly interacting with the flagella or flagellar motor. Any slight modifications could have potentially caused drastic changes in the swimming abilities and behaviors of *E. coli* cells. In the following sections I address these possible modes of interaction. Yet another interaction could have stemmed from one of the antibacterial properties of silver, namely the production of reactive oxygen species. Reactive oxidative stress is one of the factors that can lead to a cell's deemphasis on the production of proteins required for motility [68].

One notable characteristic of the velocity data to address is the bimodality of the control distribution which was starkly different from that of the silver-treated data, specifically at hour 0. This, along with the larger error could most likely best be explained by the fact that only one control experiment was performed. Two experiments were performed for both 30 and 40 μM Ag^+. The greater number of samples would decrease the standard error of the mean. Another possible explanation could be the existence of multiple phenotypes in the culture that display different running speeds. Nonetheless, the phenotype responsible for the peak seen in the silver-treatment experiments was present in the control as well.

Beyond changes to the magnitude of the swimming velocity, the presence of Ag^+ was also seen to affect the shape of the cells' paths. The chord-arc ratio (CAR), as described in the methods, is a value used to compare path shapes between swimming cells. In figure 16 I plotted the CAR cumulative density functions (CDF) for each concentration and hour. The data in this plot is derived from aggregates of CAR CDFs made for each individual movie. The 50 points correspond to mean frequencies of the 50 bins used to make each of the histograms. The error bars indicate standard error. The lower right figure displays the area under each of the CAR curves for each time point and concentration. This area under the curve (AUC) can range from 0 to 1. Propagation of error was used to construct the bars.

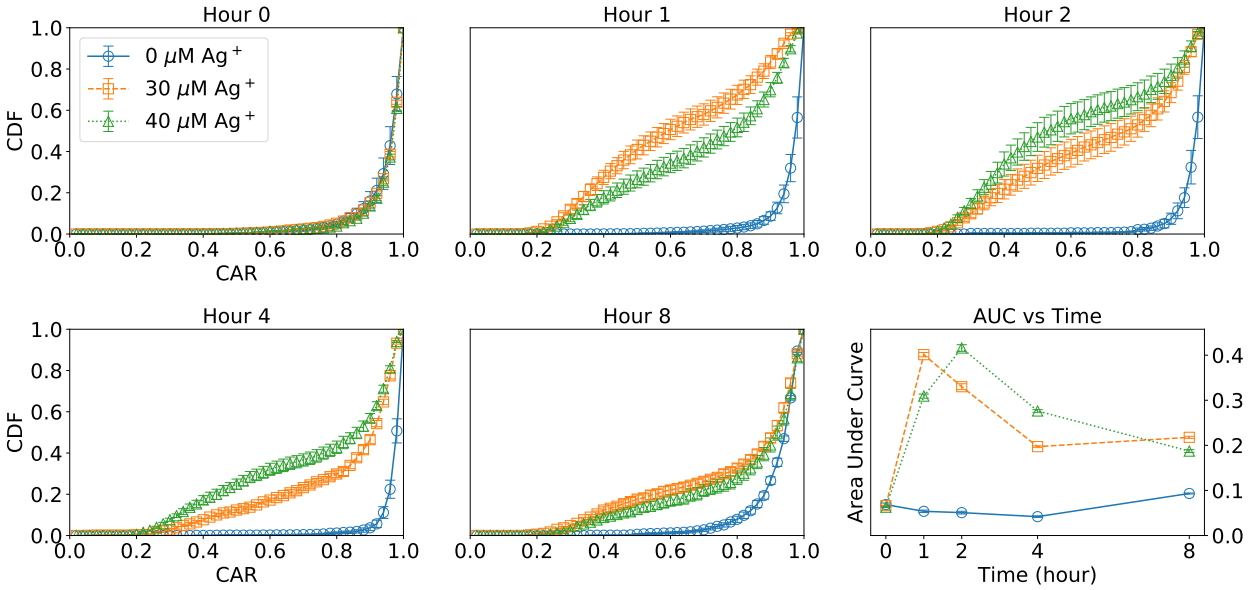

Figure 16: The cumulative density function (CDF) of the chord-arc ratios was found for each track in every movie. These CDFs were then averaged over appropriately. The standard error of the mean accompanies the mean for each of the 50 bins. Using the area under the curve (AUC) of the CAR CDF I directly compared the distributions (lower right). The CAR-AUC of the silver-treated cells increased indicating an on the whole longer path length relative to the control value. This CAR-AUC value decreased over time and eventually came close to merging with the control value.

The control data, shown in blue circles, saw very little change over the course of 8 hours. The AUC value stayed mostly constant for 4 hours until increasing to almost 0.1 at hour 8. The silver-treated cells, on the other hand, jumped up in AUC value more than 4-fold after coming into contact with silver. A high AUC value corresponds with a larger number of cells with lower CAR. The low CAR is associated with tortuous trajectories. This data implies that silver caused cell paths to become more curved as opposed to directed, and the number of curved paths decreased over time.

High trajectory tortuosity can be caused by a hugh number of reorientation events. In the context of bacterial swimmers and diffusion, reorientation events can be found during periods of tumbling or during Brownian motion. In the case of bacterial tumbling, the chord arc ratio will decrease due to the cell staying in one place and if the new swimming direction is different from the swimming direction prior to tumbling. For Brownian motion, the direction of motion will pull from a random distribution. For the results presented here it is likely that the bacteria were not switching from superdiffusion to subdiffusion, but rather are tumbling more frequently. These conclusions are supported by the results from anomalous diffusion analyses performed and the hidden Markov modeling done on tethered bacteria.

The results of the CAR analysis are independent of the velocity. To show this, take for example two trajectories of the same path but one is completed in 10 seconds and the other in 20. Both of these example trajectories will show the same CAR since there is no time dependence.

The increased tumble frequencies, as expressed by the lowered CARs, illustrate that silver ions may affect the behavior of the bacterial flagella in multiple ways. As discussed before, the dip in velocity indicates that the cells are not able to output as much power to the flagellar motor. Now, additionally, silver ions may also be disrupting the switching behavior between running and tumbling modes. This interference will cause the cell to potentially be unable to optimize its swimming direction; despite the chemotactic signalling pathway attempting to respond to the local environment, the flagella is not able to carry out those

requests because of silver ions. Further investigation into the interaction between silver ions and the flagellar motor could further elucidate the reasons for the observed behavior.

3.1.3 Diffusion Analysis Rules Out Cell Death as Cause for Observed Changes

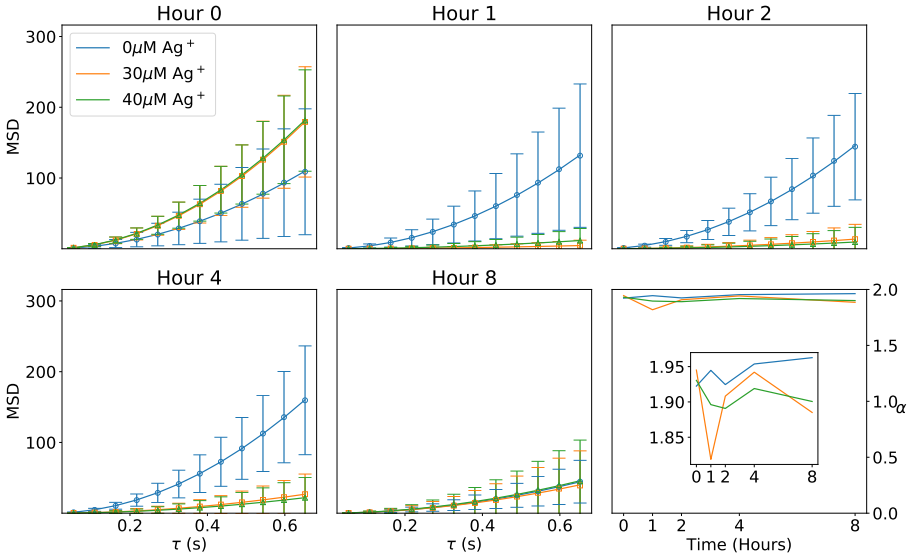

Figure 17: Mean square displacement (MSD) plotted versus lag time (τ). MSD from each trajectory was taken over maximum lag time of 12 frames (0.7 seconds) and averaged over (displayed as the data points). The error bars represent the standard deviation for each lag time. Data points were fit with equation 8 to obtain D and α. The α value of the fitted curve is plotted over time for each concentration of Ag^+ (lower right). Although there is a slight decrease at 1 hour post-Ag^+, α remains greater than 1 (superdiffusive) for each set.

A glaring concern to address is the possibility of silver killing the bacteria at these concentrations. These dead cells would be seen to have a slower swimming velocity and a higher tumbling rate due to effects of Brownian motion. Killed cells will simply diffuse rather than superdiffuse. To find the cells' diffusion class I found the MSD vs lag-time for each track and fit the ensemble-averaged data to equation 9. The results from that fitting are shown in figure 17. Here, I have shown that the first 12 points of the combined data fit the mathematical model very tightly. From this fit I found the diffusivity constant α for each set of data and plotted those values versus time. Clearly, none of the data sets show a decrease below $\alpha = 1$, which would imply pure diffusion. The value of α does decrease,

though, indicating that silver ions may have caused some of the cells to be killed, but most retain the same diffusivity class (i.e. superdiffusion).

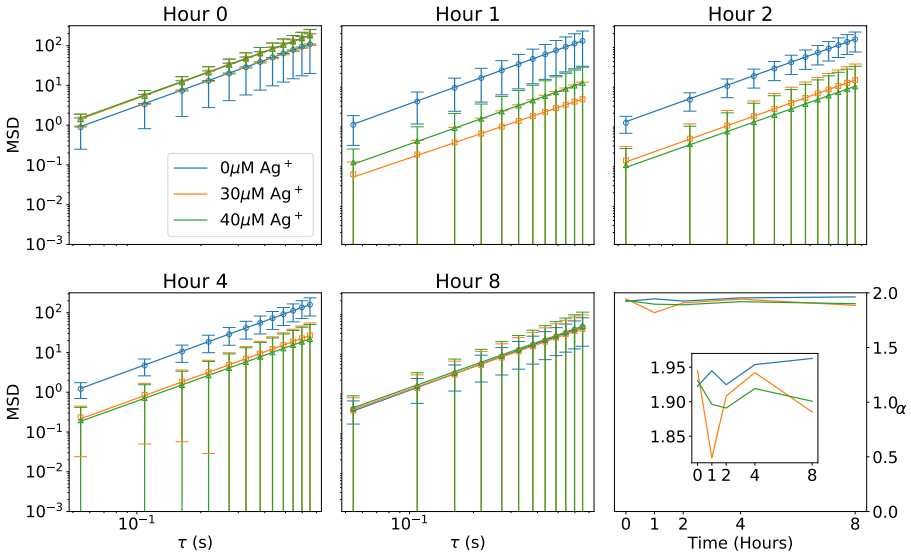

Figure 18: Log-log scaled plot of data from figure 17.

Figure 18 shows the same MSD data versus τ plotted in log-log scale. In this scale the data is linear with α as the slope and the y-intercept is related to the diffusion coefficient D by equation 10. From this figure, it is clear to see that the diffusion coefficient decreased after the introduction of silver and finally merged with the control values at hour 8. This result for D is redundant with the result from swimming velocity.

3.2 Tethering Assay Experiments

3.2.1 Silver Changes Shape of Rotational Velocity Distribution

The rotational velocity of a tethered cell can be used to probe the cell's response to external substances. *E. coli* cells were tethered to the glass coverslip bottom of a culture dish. I calculated the rotational velocity over time of each cell both before and after adding silver ions. Figure 19 shows that data from two model cells, one treated with silver and one treated with the same volume of pure media. The pre-silver distributions show a clear bimodality. These two states, one at a large positive ω value and the other centered around 0, can be

seen to represent the running and tumbling states of free-swimming cells. After treatment with silver, the distribution shifted from having two modes to displaying only one. This preliminary result agrees with the results of the free-swimming experiments.

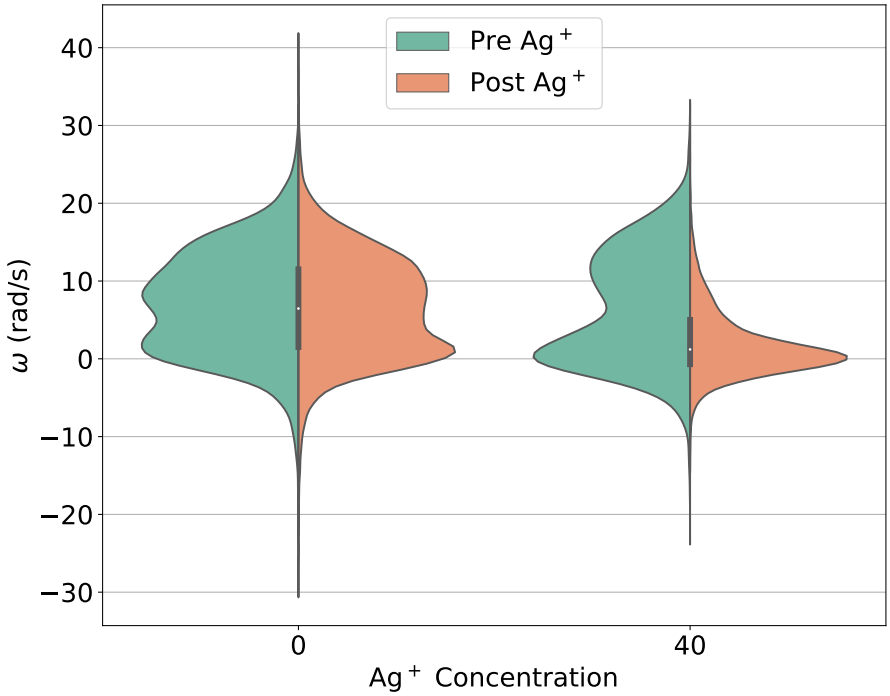

Figure 19: Histograms of the rotational velocities of two exemplary cells are shown here. The control cell (left) shows no significant changes in the distribution of ω between the pre- and post-Ag^+ data. The silver-treated cell (right) displays a change from a bimodal distribution of ω to a unimodal one. This visualization appears to suggest that the tumbling mode dominates after the addition of silver.

The disappearance of the faster rotation mode is well explained by the same possible sources mentioned in previous discussion. This data, however, provides increased robustness as the same cell is imaged both before and after the addition of silver. This fact proves that the change in behavior is indeed caused by silver and not just an artifact of data aggregation.

The time dependency of silver ions' effect on silver was also examined. In figure 20, I have plotted the ω versus time values for the same two exemplary cells used in figure 19. The top row shows the control cell, and the bottom row shows the silver ion-treated cell. The colored data is the rolling mean of ω with a windows size of 12 points, and the gray

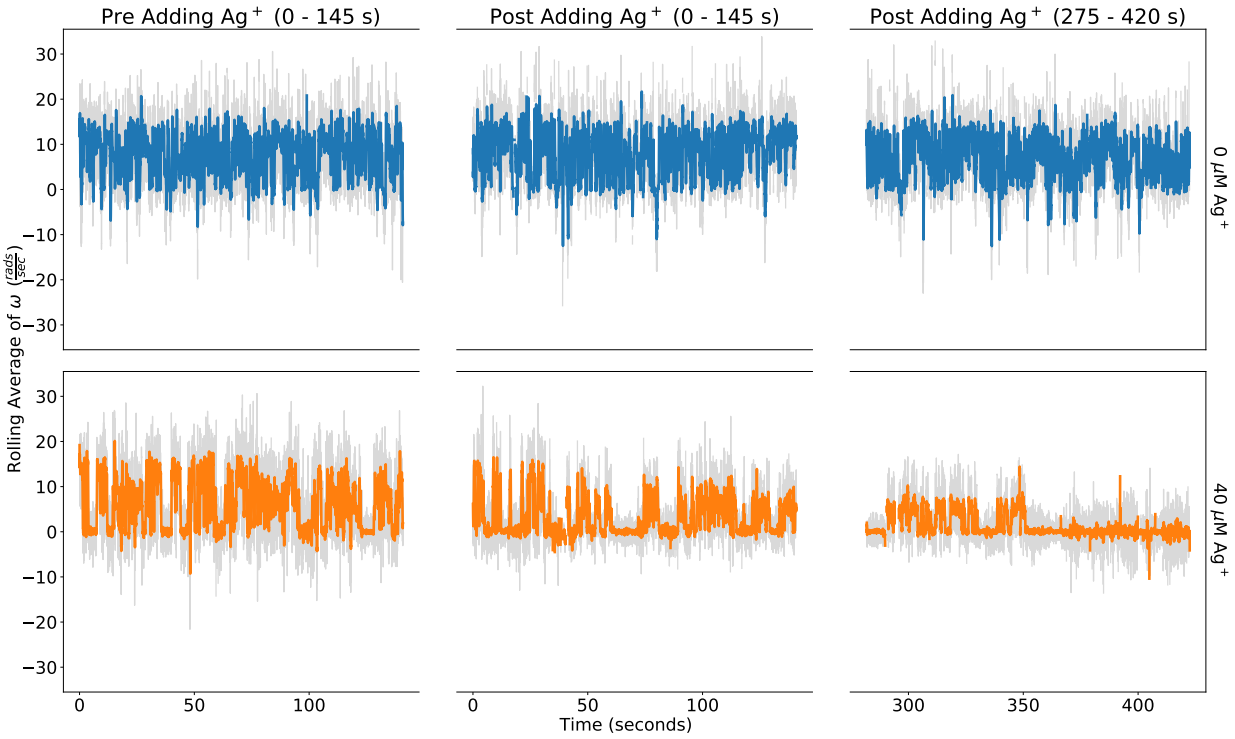

Figure 20: Using the same cells from figure 19, I also plotted the rotational velocity of each cell versus time. The gray lines show the raw data, and the colored lines show the rolling mean (window size of 12 frames). The first column of figures (left) shows the pre-Ag^+ data, and the latter two columns display the ω data after silver was added. The top row belongs to the control cell, and bottom to the silver-treated cell. About five minutes after silver was added to the culture dish the cell appears to rotate solely in the slower mode, which we assume to be the tumbling state.

background is the raw data. As evident by the middle column, after silver was added to the dish the previous bimodal switching steadily changed to a switching between a tumbling mode and a slower running mode. Eventually, as shown in the right column, ∼6 minutes after the addition of silver ions the ω value remained almost solely around 0 rad/s.

The length of time recorded in this experiment was far less than that of the free-swimming experiment; rather than hours, data collection for the tethering assays extended to about 25 minutes after inoculation. The results here show that silver changed two key components of the rotational behavior of *E. coli*: the rotational velocity and the distribution of the two modes. The former conclusion is consistent with the results of the free-swimming experiments during which the velocity was seen to decrease immediately after treatment with silver. The latter point corroborates with the result from the CAR analysis of the free-swimming experiment; the tumbling frequency is seen to increase and running frequency decrease.

3.2.2 Silver Ions Cause Significant Changes to Parameters in Hidden Markov Model of Rotational Velocity

To further investigate the time-dependent behavior of the rotational velocity switching, I modeled the two-state system (consisting of running and tumbling) as a hidden Markov process with rotational velocity as the Gaussian emissions. By fitting the model to the pre-silver data points I was able to use that model to make predictions as to the states of the post-silver data points. The prediction results are shown in figure 21. This is the same data used for figure 20.

As seen here, when comparing the control and silver-treated samples, both appeared very similar before the point when silver was added (green vertical lines). The running and tumbling states are shown in yellow and purple, respectively. The points labeled running clearly correspond to the high positive ω peak seen in figure 19, and the tumbling to the zero-centered mode. Gaps in the data correspond to frames that were removed due to the presence of one or more other cells within ROI.

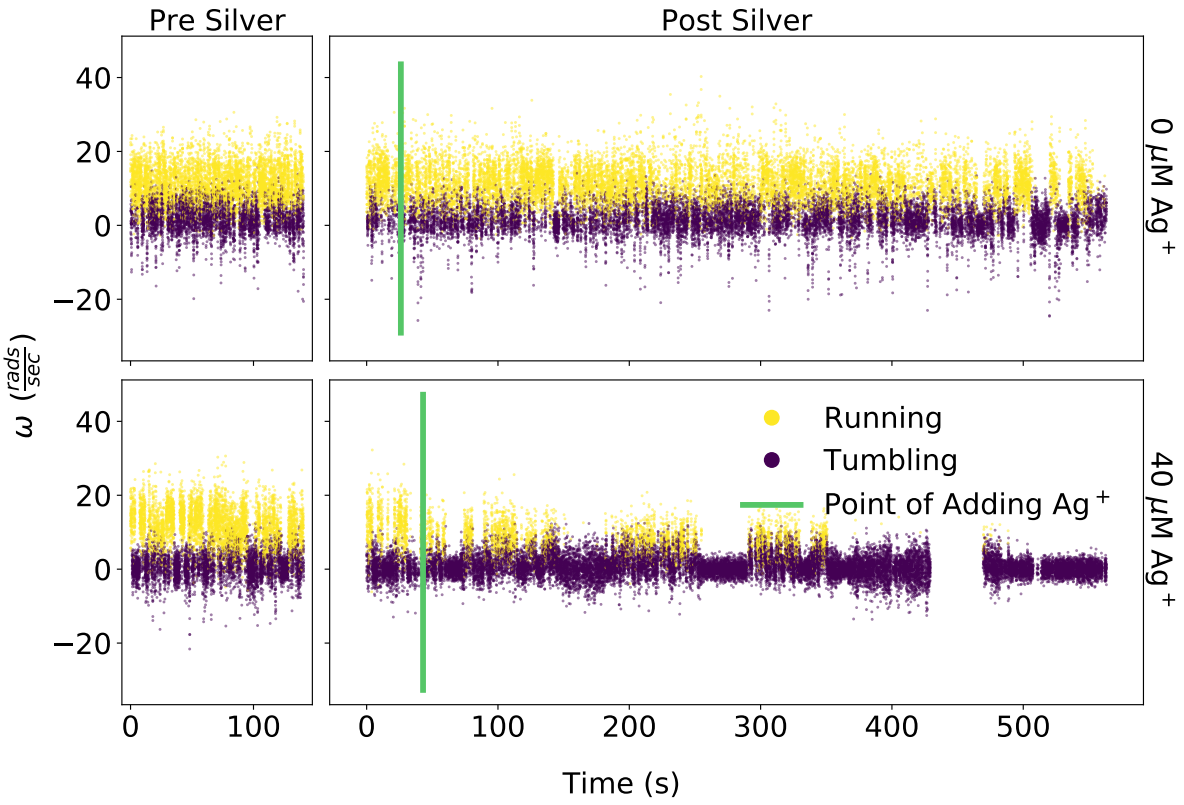

Figure 21: Here, I used the hidden Markov models created by fitting against the pre-Ag^+ data from both concentrations to predict the states of the corresponding post-Ag^+ data. The predicted labels 'Running' and 'Tumbling' are color-coded with yellow and purple, respectively. Before adding Ag^+, the distribution of states seemed to be very similar between both samples. However, a few minutes after being treated with silver the second sample became dominated by the tumbling state. Gaps in data are products of frames removed because of interference (e.g. by other cells entering the imaging ROI).

The transition matrix and stationary distribution of the HMM were clearly not the same for the silver-treated cell. Here, the presence of silver ions was seen to decrease the stationary distribution of the running state (π_{Run}) and increase the tumble-to-tumble probability ($A_{\text{Tumble}\to\text{Tumble}}$). This data also revealed a new result in the observation that the length of tumbling times is also increased. The previous analysis of the CARs only revealed the prevalence of increased running frequency. Here, it is also clear that tumbling times were extended (see t=250 to 300 s in silver-treated cell).

This result is shown more robustly by visualizing the percentage changes in HMM parameters between the pre- and post-silver prediction arrays. Here, 17 silver-treated and 10 untreated tethered cells were analyzed. Using HMM models trained on the pre-silver data for each cell, the hidden states of the post-treatment data were found using the predictive power of the pre-silver model. From these predictions, the stationary distribution and transition matrix after silver were found by calculating each of the probabilities over a 10,000 frame window ($\sim$140s, 5000 frame stride). Using these derived parameters in each of the 20 windows, I then found the percentage changes of these parameters relative to the pre-silver HMM parameters. Error bars are standard error.

The three parameters displayed here are the transition probability from tumble to run ($A_{Tumble\to Run}$, left), the transition probability from run to run ($A_{Run\to Run}$, middle), and the stationary distribution of run to run (π_{Run}). $A_{Tumble\to Run}$ decreased for both control and silver-treated experiments, but silver-treated values decreased much more drastically. This change supports the conclusion that the length of tumbling periods becomes longer after the addition of silver; cells are less likely to switch out of the tumbling mode and thus those modes will be longer. $A_{Run\to Run}$ initially does not show much change. Eventually, about 9 minutes after treatment time, the run-to-run probability of silver-treated cells begins to skew negative. Note that the standard error also increases around this same time implying that there is greater heterogeneity in this value. Additionally, some cells became untethered after a few minutes so the number of samples decreases (this could also have affected the standard

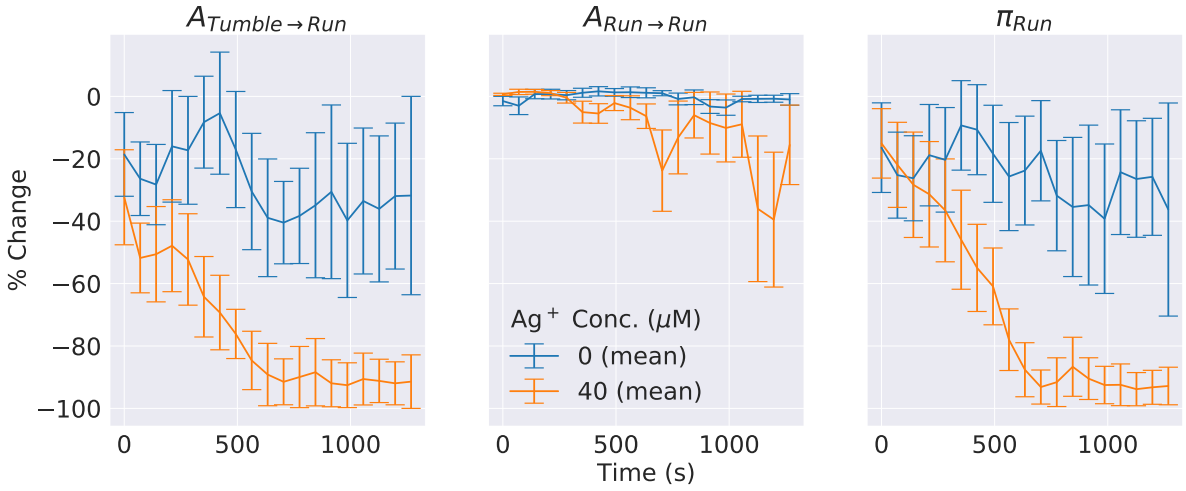

Figure 22: Percentage changes in HMM parameters after treatment with silver. Data points were obtained by predicting on the post-silver data, extracting the parameters (such as the transition matrix A and stationary distribution π) from a windowed subsample of predictions (window size of 10k frames, stride of 5k frames), finding the percentage change of those parameters with respect to the pre-Ag^+ parameters for each sample, and finally calculating relevant statistics (mean and standard error are shown here) on the appropriately ensembled data. As shown here, the percentage drop of the transition probability from the tumbling state to running state (left) was far greater for silver-treated samples than for the control samples. This drop was even more pronounced as time went on. The transition probability from run to run (middle) did not see as large a divergence between the controls and positive samples. Finally, the stationary probability of the running state decreased dramatically when compared to the change seen in the control (right).

error). The finding that $A_{Run \to Run}$ does not change much with time is intriguing. This result implies that cells are not able to break out of the tumbling mode once switched into it but can stay in the running mode relatively unincumbered. Finally, the stationary distribution of the running mode was seen to decrease very quickly for the silver-treated samples yet only slightly decrease for the control experiments. This result follows from previous points made; cells unable to escape the tumbling mode of rotation will not get the opportunity to run. This result also agrees with the free-swimming results that showed a higher frequency of tumbling when compared to the controls

4 Conclusion

Although silver has been known to possess antimicrobial properties for thousands of years, its multi-faceted effect on bacteria is only recently gaining a more full explanation. Furthermore, as silver nanoparticles become more common place in medical and consumer devices, the interactions between silver ions and bacteria must be more completely understood. The work done in this research represents a newly investigated means of disruption of *E. coli* cells. Here, silver ions were shown to possess potent anti-motility effects. Cells under duress of silver ions were seen to decrease swimming velocity and increase tumble frequency and tumble duration. These results stemmed directly from analysis of swimming and tethered bacteria in the presence of varying concentrations of silver ions. It was shown that the concentrations used in this experiment did not display many differences in the severity of their effects. Elapsed time from treatment time proved to be integral to the effects on *E. coli* swimming velocity, track tortuosity, and fitted HMM parameters; cells are most affected soon (30 to 60 minutes) after the addition of silver ions to culture media. The quantitative results obtained here are greatly important for using silver substances as antimicrobials.

Motility and the swimming velocity are vital tools for bacterial cells. The results seen here suggest that silver ions have a detrimental effect on the motility of *E. coli* cells. These findings have direct consequences on the virulent power of motile *E. coli*; cells in the presence of silver ions will have a lesser ability to scavenge for nutrients, a worse chance of fleeing from toxins or antibiotics, and a weakened arsenal with which to create biofilms. Biofilms, one of the more difficult forms of infections to treat, are partially dependent on motility to form. Therefore, understanding how silver can be used to prevent this mode of virulence should be of great interest for future research and manufacturing applications. Furthermore as silver nanoparticles, whose primary antibacterial mechanism is the release of silver ions, are used at an increasing rate for surface disinfection the results obtained here represent important discoveries in furthering the understanding of silver ions and nanoparticles as antibacterials.

5 References

[1] Aishwarya J. Ramalingam. History of antibiotics and evolution of resistance. *Research Journal of Pharmacy and Technology*, 8(12):1719–1724, 12 2015. Copyright - Copyright A&V Publications Dec 2015; Last updated - 2016-01-14.

[2] Jessica M. A. Blair, Mark A. Webber, Alison J. Baylay, David O. Ogbolu, and Laura J. V. Piddock. Molecular mechanisms of antibiotic resistance. *Nature Reviews.Microbiology*, 13(1):42–51, 01 2015.

[3] C. Lee Ventola. The antibiotic resistance crisis: part 1: causes and threats. *P & T : a peer-reviewed journal for formulary management*, 40(4):277–283, Apr 2015. 25859123[pmid].

[4] Julian Davies and Dorothy Davies. Origins and evolution of antibiotic resistance. *Microbiology and Molecular Biology Reviews*, 74(3):417–433, 2010.

[5] Alexander Fleming. On the antibacterial action of cultures of a penicillium, with special reference to their use in the isolation of b. influenzæ. *British journal of experimental pathology*, 10(3):226–236, Jun 1929. PMC2048009[pmcid].

[6] Gregory L. Armstrong, Laura A. Conn, and Robert W. Pinner. Trends in Infectious Disease Mortality in the United States During the 20th Century. *JAMA*, 281(1):61–66, 01 1999.

[7] E. P. Ab and E. Chain. An enzyme from bacteria able to destroy penicillin. *Nature*, 146(3713):837–837, 1940.

[8] Vanessa M. D'Costa, Christine E. King, Lindsay Kalan, Mariya Morar, Wilson W. L. Sung, Carsten Schwarz, Duane Froese, Grant Zazula, Fabrice Calmels, Regis Debruyne, G. Brian Golding, Hendrik N. Poinar, and Gerard D. Wright. Antibiotic resistance is ancient. *Nature*, 477:457 EP –, Aug 2011.

[9] J. Davies, W. Gilbert, and L. Gorini. Streptomycin, suppression, and the code. *Proceedings of the National Academy of Sciences of the United States of America*, 51(5):883–890, May 1964. 14173007[pmid].

[10] D. J. Tipper and J. L. Strominger. Mechanism of action of penicillins: a proposal based on their structural similarity to acyl-d-alanyl-d-alanine. *Proceedings of the National Academy of Sciences of the United States of America*, 54(4):1133–1141, Oct 1965. 5219821[pmid].

[11] Majed M. Masadeh, Karem H. Alzoubi, Omar F. Khabour, and Sayer I. Al-Azzam. Ciprofloxacin-induced antibacterial activity is attenuated by phosphodiesterase inhibitors. *Current Therapeutic Research*, 77:14 – 17, 2015.

[12] Sibhghatulla Shaikh, Jamale Fatima, Shazi Shakil, Syed Mohd Danish Rizvi, and Mohammad Amjad Kamal. Antibiotic resistance and extended spectrum beta-lactamases:

Types, epidemiology and treatment. *Saudi journal of biological sciences*, 22(1):90–101, Jan 2015.

[13] Alvaro San Millan. Evolution of plasmid-mediated antibiotic resistance in the clinical context. *Trends in Microbiology*, 26(12):978 – 985, 2018.

[14] I. M. Gould. A review of the role of antibiotic policies in the control of antibiotic resistance. *Journal of Antimicrobial Chemotherapy*, 43(4):459–465, 04 1999.

[15] Stacy Sneeringer, James MacDonald, Nigel Key, William McBride, and Ken Mathews. Economics of antibiotic use in u.s. livestock production. Technical Report ERR-200, United States Department of Agriculture, 11 2015.

[16] Eric D. Brown and Gerard D. Wright. Antibacterial drug discovery in the resistance era. *Nature*, 529:336 EP –, Jan 2016.

[17] Infectious Diseases Society of America (IDSA), Brad Spellberg, Martin Blaser, Robert J. Guidos, Helen W. Boucher, John S. Bradley, Barry I. Eisenstein, Dale Gerding, Ruth Lynfield, L. Barth Reller, John Rex, David Schwartz, Edward Septimus, Fred C. Tenover, and David N. Gilbert. Combating antimicrobial resistance: policy recommendations to save lives. *Clinical infectious diseases : an official publication of the Infectious Diseases Society of America*, 52 Suppl 5(Suppl 5):S397–S428, May 2011. 21474585[pmid].

[18] Mathew Renwick and Elias Mossialos. What are the economic barriers of antibiotic r&d and how can we overcome them? *Expert Opinion on Drug Discovery*, 13(10):889–892, 2018. PMID: 30175625.

[19] Mahendra Rai, Alka Yadav, and Aniket Gade. Silver nanoparticles as a new generation of antimicrobials. *Biotechnology Advances*, 27(1):76 – 83, 2009.

[20] J. Wesley Alexander. History of the medical use of silver. *Surgical Infections*, 10(3):289–292, 2009. PMID: 19566416.

[21] Svitlana Chernousova and Matthias Epple. Silver as antibacterial agent: Ion, nanoparticle, and metal. *Angewandte Chemie International Edition*, 52(6):1636–1653, 2 2013.

[22] Tianlu Zhang, Liming Wang, Qiang Chen, and Chunying Chen. Cytotoxic potential of silver nanoparticles. *Yonsei medical journal*, 55(2):283–291, Mar 2014. 24532494[pmid].

[23] Xi-Feng Zhang, Zhi-Guo Liu, Wei Shen, and Sangiliyandi Gurunathan. Silver nanoparticles: Synthesis, characterization, properties, applications, and therapeutic approaches. *International Journal of Molecular Sciences*, 17(9):1534, Sep 2016.

[24] Okkyoung Choi, Kathy Kanjun Deng, Nam-Jung Kim, Louis Ross, Rao Y. Surampalli, and Zhiqiang Hu. The inhibitory effects of silver nanoparticles, silver ions, and silver chloride colloids on microbial growth. *Water Research*, 42(12):3066 – 3074, 2008.

[25] Nelson Durán, Priscyla D. Marcato, Roseli De Conti, Oswaldo L. Alves, Fabio T. M. Costa, and Marcelo Brocchi. Potential use of silver nanoparticles on pathogenic bacteria, their toxicity and possible mechanisms of action. *Journal of the Brazilian Chemical Society*, 21:949 – 959, 00 2010.

[26] Q. L. Feng, J. Wu, G. Q. Chen, F. Z. Cui, T. N. Kim, and J. O. Kim. A mechanistic study of the antibacterial effect of silver ions on escherichia coli and staphylococcus aureus. *Journal of Biomedical Materials Research*, 52(4):662–668, 2000.

[27] Gianluigi Franci, Annarita Falanga, Stefania Galdiero, Luciana Palomba, Mahendra Rai, Giancarlo Morelli, and Massimiliano Galdiero. Silver nanoparticles as potential antibacterial agents. *Molecules*, 20(5):8856–8874, 2015.

[28] Chun-Nam Lok, Chi-Ming Ho, Rong Chen, Qing-Yu He, Wing-Yiu Yu, Hongzhe Sun, Paul Kwong-Hang Tam, Jen-Fu Chiu, and Chi-Ming Che. Proteomic analysis of the mode of antibacterial action of silver nanoparticles. *Journal of Proteome Research*, 5(4):916–924, Apr 2006.

[29] Jose Ruben Morones, Jose Luis Elechiguerra, Alejandra Camacho, Katherine Holt, Juan B Kouri, Jose Tapia Ramírez, and Miguel Jose Yacaman. The bactericidal effect of silver nanoparticles. *Nanotechnology*, 16(10):2346–2353, aug 2005.

[30] Humberto H. Lara, Nilda V. Ayala-Nú nez, Liliana del Carmen Ixtepan Turrent, and Cristina Rodríguez Padilla. Bactericidal effect of silver nanoparticles against multidrug-resistant bacteria. *World Journal of Microbiology and Biotechnology*, 26:615–621, apr 2010.

[31] Gaurav Pal, Priya Rai, and Anjana Pandey. Chapter 1 - green synthesis of nanoparticles: A greener approach for a cleaner future. pages 1 – 26, 2019.

[32] Sang Hun Lee and Bong-Hyun Jun. Silver nanoparticles: Synthesis and application for nanomedicine. *International journal of molecular sciences*, 20(4):865, Feb 2019. 30781560[pmid].

[33] J. Jang, H.-G. Hur, M.J. Sadowsky, M.N. Byappanahalli, T. Yan, and S. Ishii. Environmental escherichia coli: ecology and public health implicationsa review. *Journal of Applied Microbiology*, 123(3):570–581, 2017.

[34] R Bentley and R Meganathan. Biosynthesis of vitamin k (menaquinone) in bacteria. *Microbiology and Molecular Biology Reviews*, 46(3):241–280, 1982.

[35] S. Hudault, J. Guignot, and A. L. Servin. Escherichia coli strains colonising the gastrointestinal tract protect germfree mice against salmonella typhimurium infection. *Gut*, 49(1):47–55, Jul 2001. 11413110[pmid].

[36] Einat Tamar, Moriah Koler, and Ady Vaknin. The role of motility and chemotaxis in the bacterial colonization of protected surfaces. *Scientific Reports*, 6:19616 EP –, Jan 2016. Article.

[37] S.C. Clarke, R.D. Haigh, P.P.E. Freestone, and P.H. Williams. Enteropathogenic escherichia coli infection: history and clinical aspects. *British Journal of Biomedical Science*, 59(2):123–127, 2002. PMID: 28700856.

[38] Angela R. Melton-Celsa. Shiga toxin (stx) classification, structure, and function. *Microbiology spectrum*, 2(4):10.1128/microbiolspec.EHEC–0024–2013–2013, Aug 2014. 25530917[pmid].

[39] Enterotoxigenic e. coli (etec). `https://www.cdc.gov/ecoli/etec.html`, Dec 2014.

[40] P. Kaur, A. Chakraborti, and A. Asea. Enteroaggregative escherichia coli: An emerging enteric food borne pathogen. *Interdisciplinary perspectives on infectious diseases*, 2010:254159–254159, 2010. 20300577[pmid].

[41] Alain L. Servin. Pathogenesis of human diffusely adhering escherichia coli expressing afa/dr adhesins (afa/dr daec): Current insights and future challenges. *Clinical Microbiology Reviews*, 27(4):823–869, 2014.

[42] M. J. C. van den Beld and F. A. G. Reubsaet. Differentiation between shigella, enteroinvasive escherichia coli (eiec) and noninvasive escherichia coli. *SpringerLink*, Sep 2011.

[43] Reports of selected e. coli outbreak investigations. `https://www.cdc.gov/ecoli/outbreaks.html`, Jul 2019.

[44] E. coli and food safety. `https://www.cdc.gov/features/ecoliinfection/index.html`, May 2019.

[45] Antibiotic resistance threats report and foodborne germs. `https://www.cdc.gov/narms/resources/threats.html`, Mar 2019.

[46] John S. Parkinson, Gerald L. Hazelbauer, and Joseph J. Falke. Signaling and sensory adaptation in escherichia coli chemoreceptors: 2015 update. *Trends in Microbiology*, 23(5):257 – 266, 2015. Special Issue: Microbial Translocation.

[47] Tohru Minamino and Katsumi Imada. The bacterial flagellar motor and its structural diversity. *Trends in Microbiology*, 23(5):267 – 274, 2015. Special Issue: Microbial Translocation.

[48] Yoshiyuki Sowa and Richard M. Berry. Bacterial flagellar motor. *Quarterly Reviews of Biophysics*, 41(2):103132, 2008.

[49] Christine Josenhans and Sebastian Suerbaum. The role of motility as a virulence factor in bacteria. *International Journal of Medical Microbiology*, 291(8):605 – 614, 2002.

[50] Christopher V. Gabel and Howard C. Berg. The speed of the flagellar rotary motor of escherichia coli varies linearly with protonmotive force. *Proceedings of the National Academy of Sciences*, 100(15):8748–8751, 2003.

[51] M. Siva Kumar and P. Philominathan. The physics of flagellar motion of e. coli during chemotaxis. *Biophysical reviews*, 2(1):13–20, Feb 2010.

[52] Timothy R. Corle and Gordon S. Kino. Confocal scanning optical microscopy and related imaging systems. 1996.

[53] Introduction to phase contrast microscopy. `https://www.microscopyu.com/techniques/phase-contrast/introduction-to-phase-contrast-microscopy`.

[54] Mohammad Aminul Haque. Experiment-based quantitative modeling for the antibacterial activity of silver nanoparticles. *Theses and Dissertations*, (2445), 2017.

[55] Rob Phillips, Jane Kondev, and Julie Theriot. *Physical Biology of the Cell*. Garland Science, Taylor & Francis Group, New York, November 2008.

[56] Willow R. DiLuzio, Linda Turner, Michael Mayer, Piotr Garstecki, Douglas B. Weibel, Howard C. Berg, and George M. Whitesides. Escherichia coli swim on the right-hand side. *Nature*, 435(7046):1271–1274, 2005.

[57] Hai-Chao Han. Twisted blood vessels: symptoms, etiology and biomechanical mechanisms. *Journal of vascular research*, 49(3):185–197, 2012. 22433458[pmid].

[58] Simon Benhamou. How to reliably estimate the tortuosity of an animal's path: straightness, sinuosity, or fractal dimension? *Journal of theoretical biology*, Jul 2004.

[59] M. Ben Clennell. Tortuosity: a guide through the maze. *Geological Society, London, Special Publications*, 122(1):299–344, 1997.

[60] Alex Eli Pottash, Ryan McKay, Chelsea R. Virgile, Hana Ueda, and William E. Bentley. Tumblescore: Run and tumble analysis for low frame-rate motility videos. *BioTechniques*, 62(1):31–36, 2017. PMID: 28118813.

[61] Pauli Virtanen, Ralf Gommers, Travis E. Oliphant, Matt Haberland, Tyler Reddy, David Cournapeau, Evgeni Burovski, Pearu Peterson, Warren Weckesser, Jonathan Bright, Stéfan J. van der Walt, Matthew Brett, Joshua Wilson, K. Jarrod Millman, Nikolay Mayorov, Andrew R. J. Nelson, Eric Jones, Robert Kern, Eric Larson, CJ Carey, İlhan Polat, Yu Feng, Eric W. Moore, Jake Vand erPlas, Denis Laxalde, Josef Perktold, Robert Cimrman, Ian Henriksen, E. A. Quintero, Charles R Harris, Anne M. Archibald, Antônio H. Ribeiro, Fabian Pedregosa, Paul van Mulbregt, and SciPy 1. 0 Contributors. SciPy 1.0–Fundamental Algorithms for Scientific Computing in Python. *arXiv e-prints*, page arXiv:1907.10121, Jul 2019.

[62] Stefan van der Walt, Johannes L. Schonberger, Juan Nunez-Iglesias, Francois Boulogne, Joshua D. Warner, Neil Yager, Emmanuelle Gouillart, Tony Yu, and the scikit-image contributors. scikit-image: image processing in python. *PeerJ*, 2:e453, 6 2014.

[63] M. Vidyasagar. *Hidden Markov Processes: Theory and Applications to Biology*. Princeton University Press, 2014.

[64] Mark Stamp. A revealing introduction to hidden markov models. http://www.cs.sjsu.edu/~stamp/RUA/HMM.pdf.

[65] Matthew C. Gibson, Ankit B. Patel, Radhika Nagpal, and Norbert Perrimon. The emergence of geometric order in proliferating metazoan epithelia. *Nature*, 442(7106):1038–1041, 2006.

[66] Byung-Jun Yoon. Hidden markov models and their applications in biological sequence analysis. *Current Genomics*, 10(6):402–415, 2009.

[67] hmmlearn. https://hmmlearn.readthedocs.io/en/latest/.

[68] Kazuyuki Shimizu. Regulation systems of bacteria such as escherichia coli in response to nutrient limitation and environmental stresses. *Metabolites*, 4(1):1–35, Dec 2013. 24958385[pmid].